SYMMETRY ENERGY AND THE ISOSCALING PROPERTIES OF THE FRAGMENTS IN MULTIFRAGMENTATION OF $^{40}Ca+^{58}Ni$, $^{40}Ar+^{58}Ni$ AND $^{40}Ar+^{58}Fe$ REACTIONS

A Thesis

by

JENNIFER ANN IGLIO

Submitted to the Office of Graduate Studies of
Texas A&M University
in partial fulfillment of the requirements for the degree of

MASTER OF SCIENCE

May 2007

Major Subject: Chemistry

SYMMETRY ENERGY AND THE ISOSCALING PROPERTIES OF THE FRAGMENTS IN MULTIFRAGMENTATION OF ^{40}Ca+^{58}Ni, ^{40}Ar+^{58}Ni AND ^{40}Ar+^{58}Fe REACTIONS

A Thesis

by

JENNIFER ANN IGLIO

Submitted to the Office of Graduate Studies of
Texas A&M University
in partial fulfillment of the requirements for the degree of

MASTER OF SCIENCE

Approved by:

Chair of Committee,	Sherry Yennello
Committee Members	Joe Natowitz
	Che-Ming Ko
Head of Department	David Russell

May 2007

Major Subject: Chemistry

ABSTRACT

Symmetry Energy and the Isoscaling Properties of the Fragments in Multifragmentation of $^{40}Ca+^{58}Ni$, $^{40}Ar+^{58}Ni$ and $^{40}Ar+^{58}Fe$ Reactions. (May 2007)

Jennifer Ann Iglio, B.S., Texas A&M University

Chair of Advisory Committee: Dr. Sherry Yennello

The symmetry energy and the isoscaling properties of the fragments produced in multifragmentation of ^{40}Ar, ^{40}Ca + ^{58}Fe, ^{58}Ni reactions at 25, 33, 45 and 53 MeV/nucleon were investigated within the framework of a statistical multifragmentation model. The isoscaling parameter, α from the hot primary and cold secondary fragment yield distributions, was studied as a function of the excitation energy, isospin (neutron-to-proton asymmetry), and fragment symmetry energy.

Through changing the symmetry energy in the statistical multifragmentation model to describe the experimental data, it is observed that the isoscaling parameter α decreases with increasing excitation energy and decreases with decreasing symmetry energy. The parameter α is also observed to increase with increasing difference in the isospin of the fragmenting system. The sequential decay of the primary fragments into secondary fragments show very little influence on the isoscaling parameter when studied as a function of excitation energy. However, the symmetry energy has a strong influence on the isospin properties of the hot fragments. The results indicate that the isospin properties of the fragments produced at high excitation energy and reduced density in multifragmentation reactions are sensitive to the symmetry energy, indicating

that the properties of hot nuclei at excitation energies, densities, and isospin away from normal ground state nuclei are significantly different than those of normal (cold) nuclei at saturation density.

DEDICATION

To my mother and father

ACKNOWLEDGMENTS

I would like to thank my committee chair, Dr. Sherry Yennello for believing in me, and my committee members for their support throughout my graduate school experience. Thank you, Dinesh Shetty for your guidance throughout the course of my research.

I would also like to thank my research group and all the faculty and staff at the Texas A&M University Cyclotron Institute for wonderful memories and a great graduate school experience. This work would not have been possible with out the support in part of the Robert A. Welch Foundation through grant No. A-1266, and the Department of Energy through grant No. DE-FG03-93ER40773, thank you for your support.

Finally, special thanks go to my parents for their encouragement and support through my entire college career.

TABLE OF CONTENTS

Page

LIST OF FIGURES

Page

FIGURE

INTRODUCTION

The possibility of creating nuclear matter that is dilute and extremely asymmetric (large neutron-to-proton ratio) using beams of neutron-rich nuclei in a laboratory has generated tremendous interest in the Nuclear and Astrophysics community. Due to its varied applications, the experimental and theoretical efforts in the last decade or so have focused primarily on investigating the role of the isospin degree of freedom at non-normal nuclear density. Normal nuclear matter is nearly symmetric (similar number of neutrons and protons) and found at densities close to the saturation density ($\rho \approx 0.17$ fm^{-3}). Most of the current knowledge on the properties of nuclear matter has been gathered by studying finite nuclei that are symmetric in isospin ($N \approx Z$), cold ($T \sim 0$ MeV) and found at normal nuclear density ($\rho \approx 0.17$ fm^{-3}). It is not known how these properties change at densities, temperatures and isospin away from normal nuclear matter. Such matter is known to be routinely produced in an astrophysical environment. It is therefore important to have a clear understanding of the isospin properties of matter, to be able to explain important astrophysical phenomena, and for testing the validity of theoretical models. In order to achieve this, it is necessary to study the behavior of nuclear matter under different conditions of temperature, pressure and volume (density), and detail the functional dependence between these quantities, represented in the form of the nuclear Equation of State.

This thesis follows the style of Physical Review C.

Current theoretical models show a large uncertainty in the equation of state of asymmetric nuclear matter. Figure 1 shows the various forms of the nuclear equation of state predicted by the microscopic calculations for the symmetric and pure neutron matter.

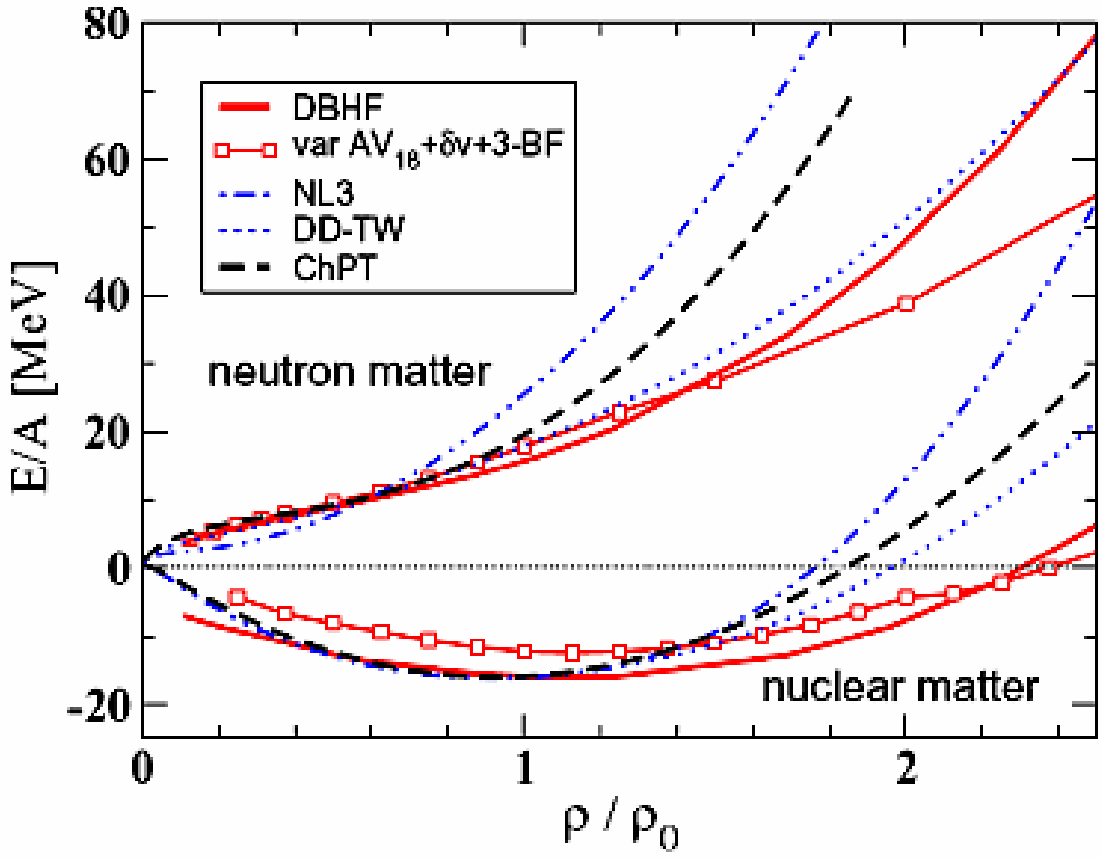

FIG. 1. Nuclear equation of state for symmetric nuclear matter and pure neutron matter as predicted by various microscopic calculations [1].

The equation of state is largely unconstrained above and below the saturation density ρ_o. The nuclear equation of state of isospin asymmetric nuclear matter can be written in a parabolic approximation by

$$E(\rho,\delta) = E(\rho,\delta = 0) + E_{sym}(\rho)\delta^2 \tag{1.1}$$

$$\delta = \frac{\rho_n - \rho_p}{\rho_n + \rho_p}, \tag{1.2}$$

where the first term in the Eq. (1.1) is the symmetric nuclear matter energy and the second term is the asymmetry energy. The quantity $E_{sym}(\delta)$ is the symmetry energy, which is defined as the energy difference between the pure neutron matter and the symmetric nuclear matter. Eq. (1.2) is the isospin asymmetry of nuclear matter, where, where ρ_n is the neutron density and ρ_p is the proton density. There exists a large uncertainty in the density dependence of the symmetry energy above and below saturation density due to the unconstrained nature of the nuclear matter equation of state. This is shown in figure 2, where various forms of the density dependence of the symmetry energy have been predicted by the microscopic calculations. In general, there are two different forms of the density dependence of the symmetry energy that have been predicted. The first is the "stiff" form, where the symmetry energy steadily increases as the density increases. The second is a "soft" form where, the symmetry energy increases initially as density increases and then starts to decrease at higher

densities. Constraining the form of symmetry energy is important in the modeling of supernova collapse and studying the structure of neutron stars.

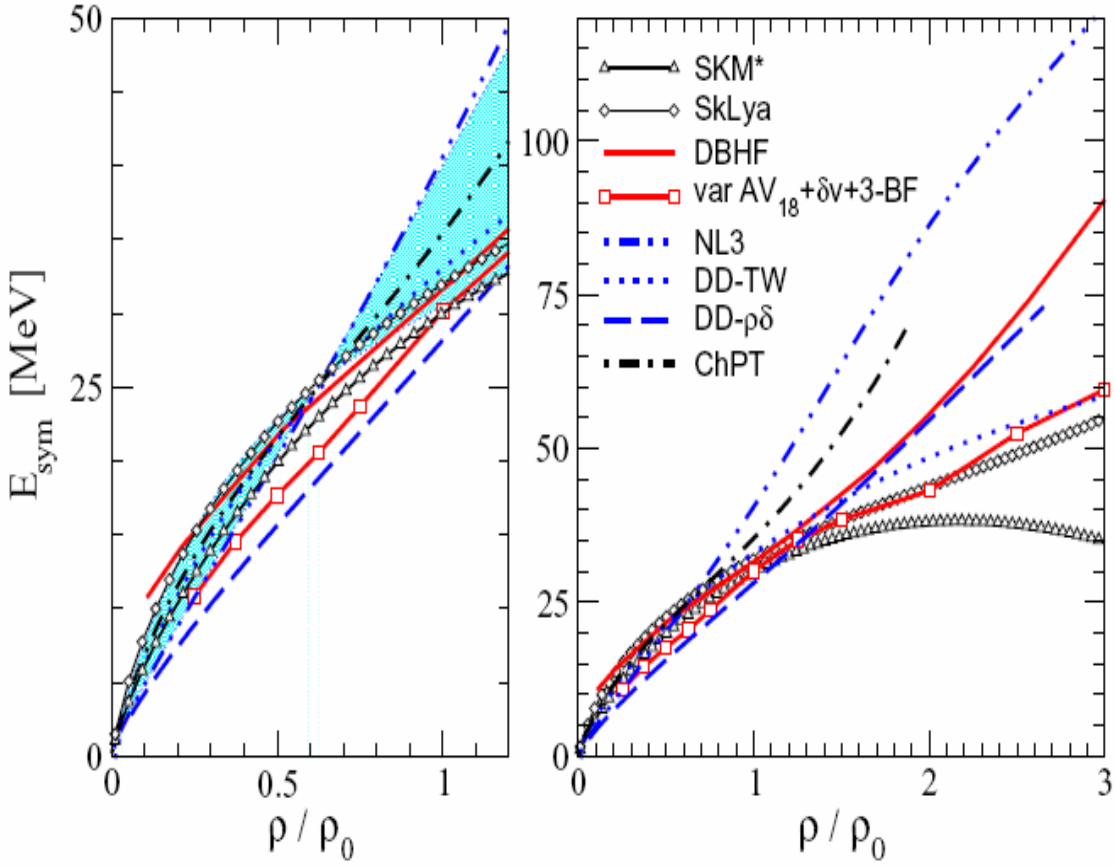

FIG. 2. Density dependence of the symmetry energy as predicted by various microscopic calculations [1].

The asymmetry term (second term in Eq. 1.1) in the nuclear equation of state is important for studying the structure, chemical compositions and evolution of neutron stars. It is also important for studying the dynamic of supernova collapse [1]. This term dominates the pressure within the neutron stars and can also modify the proton-neutron star cooling rate [1]. In a supernova explosion, the variation of the asymmetry energy can alter the rate of electron capture in a collapsing star, thereby altering the course of final explosion [1]. Figure 3 shows that for a stiff form of the density dependence of symmetry energy in the modeling of a neutron star, the proton fraction can reach a certain threshold value enabling the star to cool by the direct URCA process. The proton fraction from the "soft" form of the density dependence of the symmetry energy does not reach this threshold limit and the star must cool by the Standard Cooling method resulting in a much slower cooling rate. It has been shown by astronomers that the neutron stars do cool much faster than those expected from the Standard Cooling Process.

The form of the density dependence of symmetry energy also affects the mass-radius relationship of neutron stars. As shown in figure 4, a "stiff" form of the density dependence of the symmetry energy results in a larger mass and radius for the neutron star compared to a relatively small mass and radius as predicted by the "soft" form.

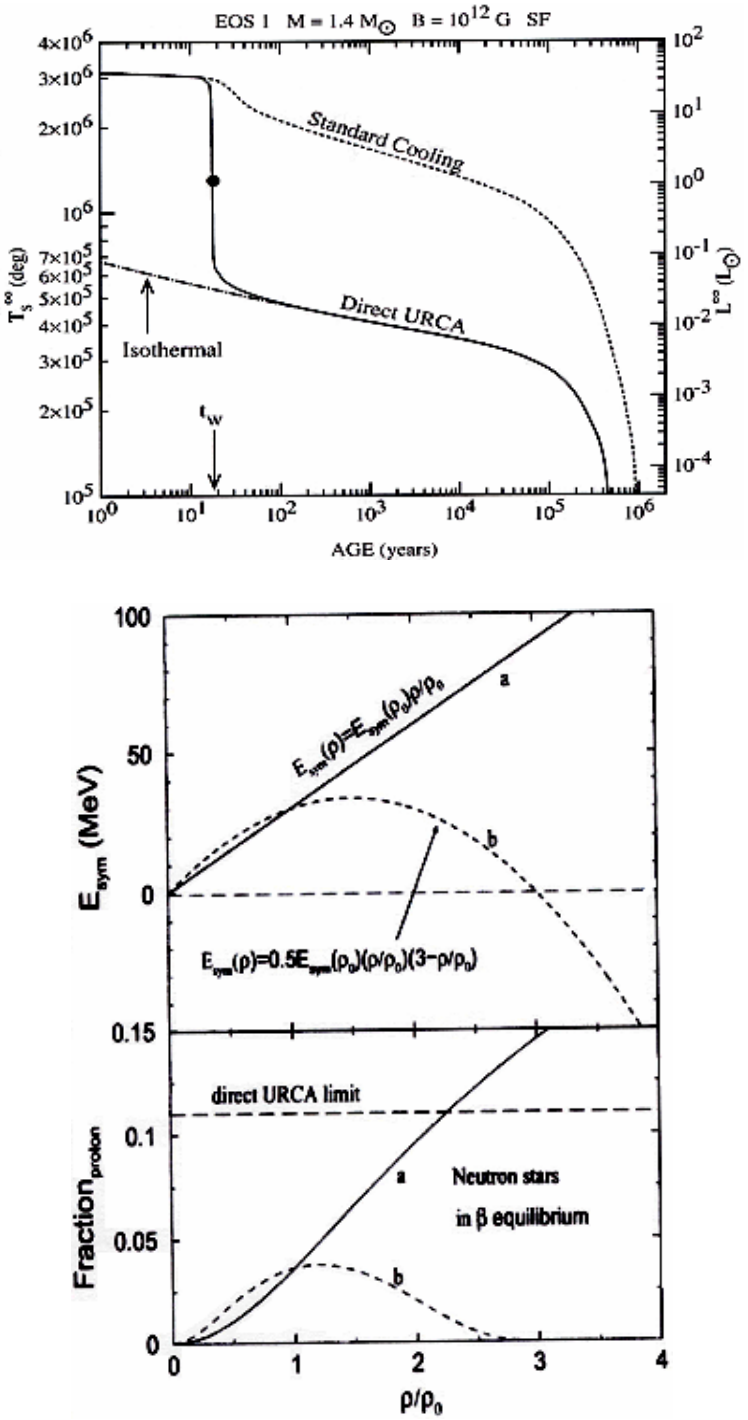

FIG. 3. Neutron star cooling and its dependence on the form of symmetry energy. The stiff form of the density dependence enables the proton fraction of a neutron star (see bottom figure) to reach a certain threshold value that is required for a star to cool by the direct URCA process. This enables it to cool much faster than those predicted by the soft form where the proton fraction does not reach the threshold limit and the star has to cool by Standard cooling method [1].

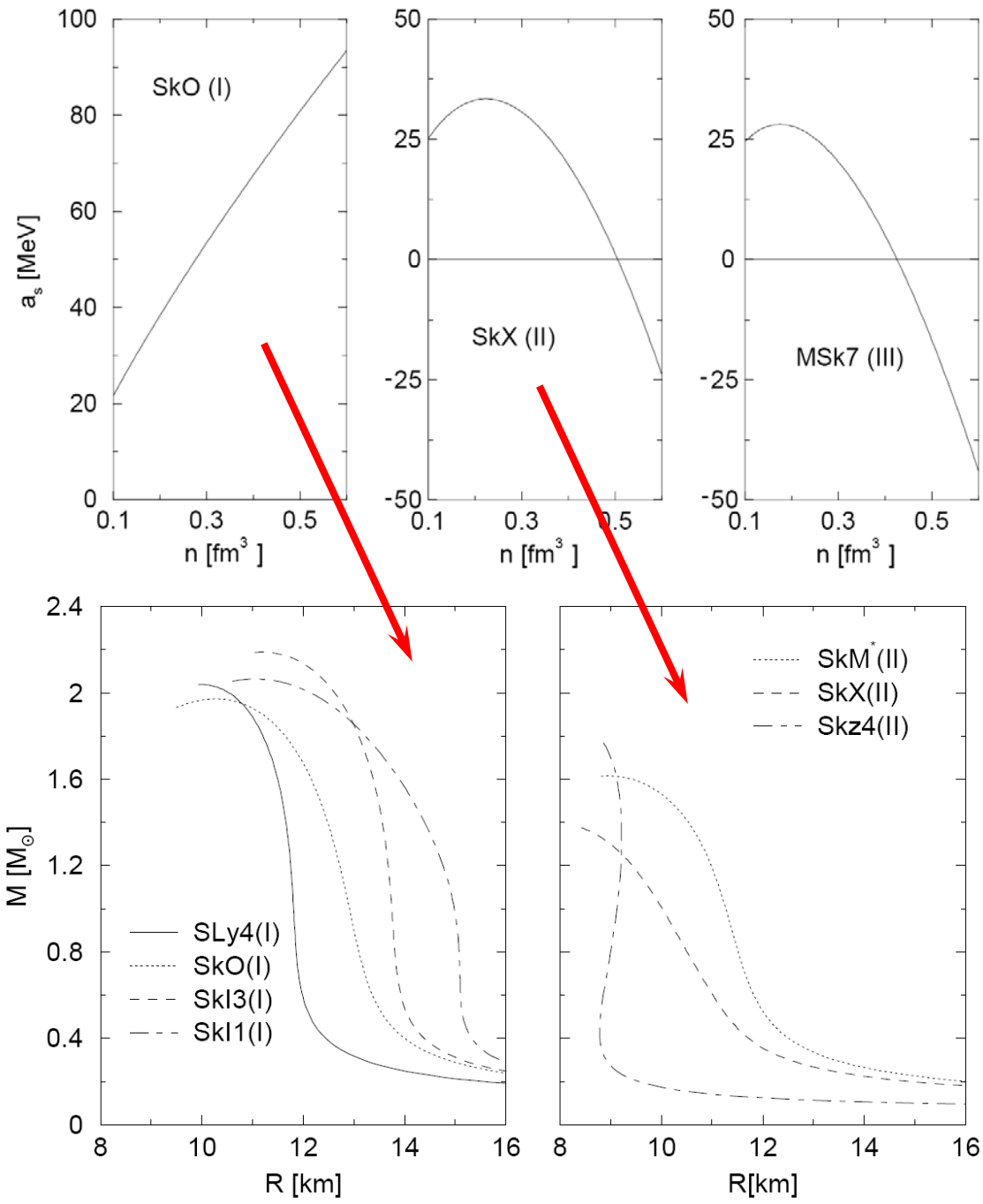

FIG. 4. The mass-radius relation of the neutron star and the form of the density dependence of the symmetry energy. The stiff form of the density dependence of the symmetry energy compared to the softer form [2].

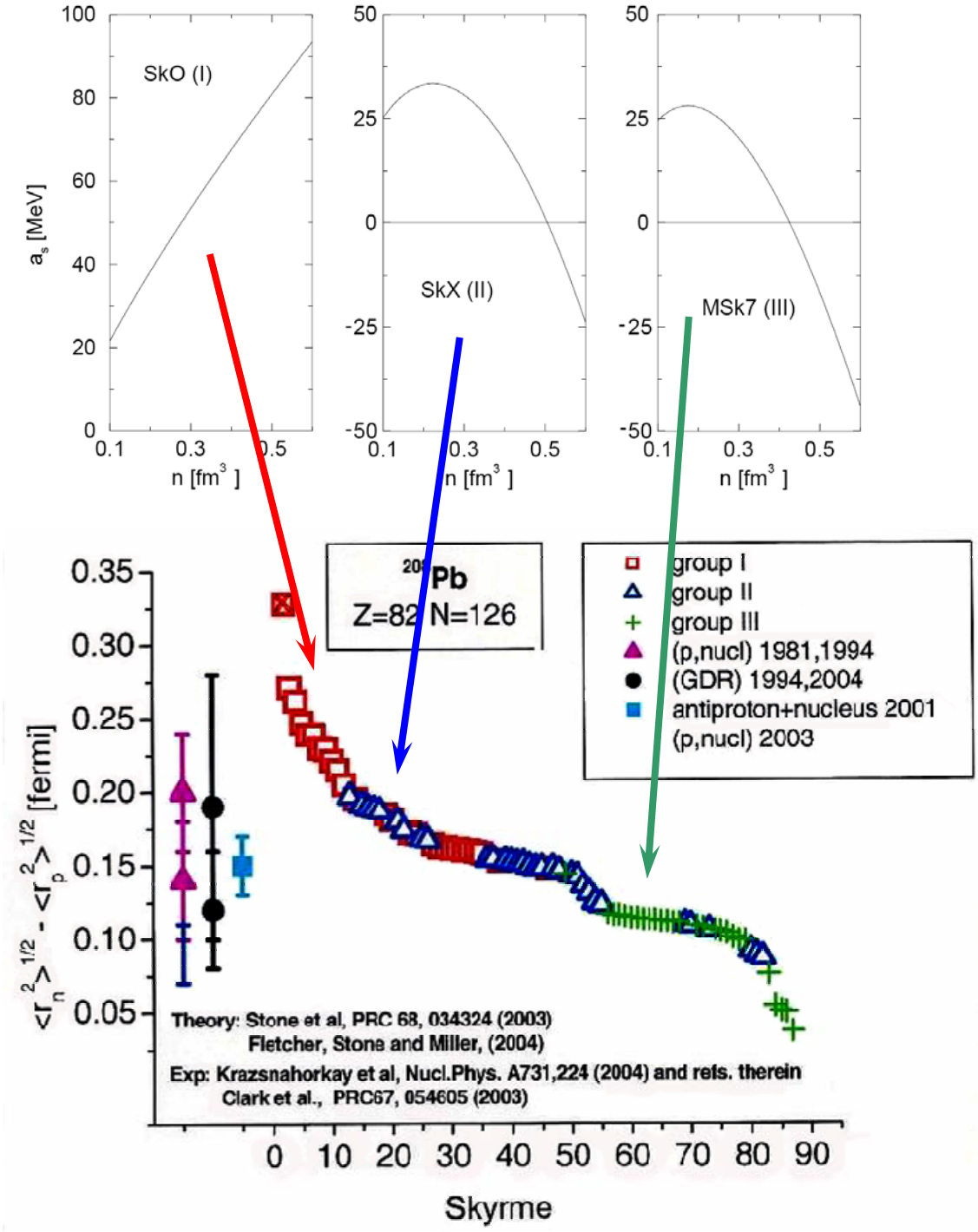

FIG. 5. The sensitivity of neutron skin thickness to the form of the symmetry energy for the ^{208}Pb nuclei. By using a "stiff" from of the symmetry energy in the calculation, a much larger neutron skin thickness is predict than those predicted by the "soft" form of the density dependence of symmetry energy [2].

Not only does the density dependence of the symmetry energy affect the cooling rate and the mass-radius relationship of neutron stars but it also determines the neutron skin thickness in ^{208}Pb nuclei. Figure 5 shows the sensitivity of the neutron skin thickness to the form of the density dependence of the symmetry energy. A larger skin thickness is predicted for the "stiff" form of the symmetry energy compared to the "soft" form of the density dependence of the symmetry energy.

Under laboratory controlled conditions, the density dependence of the symmetry energy in the low density regime can be investigated in a multifragmentation reaction, where the system expands to low density before disassembling into many light and heavy fragments. Figure 6 shows a typical sketch of a multifragmentation process. By studying the fragment isotopic yield distribution, one can extract important information about the symmetry energy.

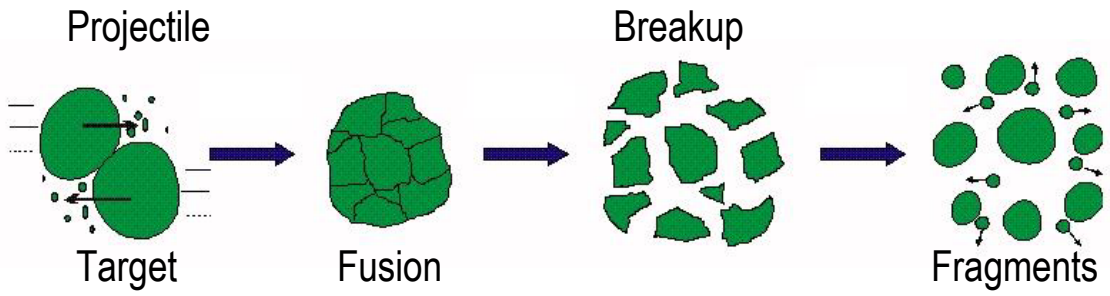

FIG. 6. A cartoon showing the process of multifragmentation. A projectile like source and a target like source collide and combine to create a compound system that fuses and becomes one. It expands until it can no longer hold together resulting in fragmentation of light and heavy particles [3].

Recently, the possibility of extracting experimental information on the symmetry energy and the isospin (neutron-to-proton ratio) of the fragments in a multifragmentation reaction has gained tremendous importance [4-8]. Such information is of importance for understanding some of the key problems in astrophysics [7,9-15], various aspects of nuclear physics such as the structure of exotic nuclei (the binding energy and rms radii) [16-19] and the dynamics of heavy ion collisions [20-27]. Traditionally, the symmetry energy has been extracted by fitting ground state binding energies with various versions of the liquid drop mass formula [28]. The properties of nuclear matter are then determined by theoretically extrapolating nuclear models that are designed to study the structure of real nuclei. However, real nuclei are cold, nearly symmetric ($N \approx Z$) and found at equilibrium density. It is not known how the symmetry energy behaves at temperatures and densities away from those of normal nuclear matter. Theoretically, many-body calculations [29-32] and those from the empirical liquid drop mass formula [33, 34] predict symmetry energy near normal nuclear density (~0.17 fm^{-3}) and temperature (T~0 MeV) to be around 28-32 MeV.

In multifragmentation reactions excited nuclei expand in a vacuum and decay into various light and heavy fragments. These fragments are highly excited and neutron rich and when emitted undergo de-excitation to cold and stable isotopes. Similar hot nuclei are also produced in the interior of a collapsing star resulting in a supernova explosion [7]. The production of these nuclei depends on their internal excitation and their sensitivity to the symmetry energy part of the binding energy [7]. It has been shown that a slight decrease in the symmetry energy co-efficient and subsequent de-excitation

can significantly alter the elemental abundance and synthesis of heavy elements [7]. This is shown in figure 7. In multifragmentation reactions, the measurement of fragment isotopic yield distributions can provide important insight into the symmetry energy and the decay characteristics of these nuclei.

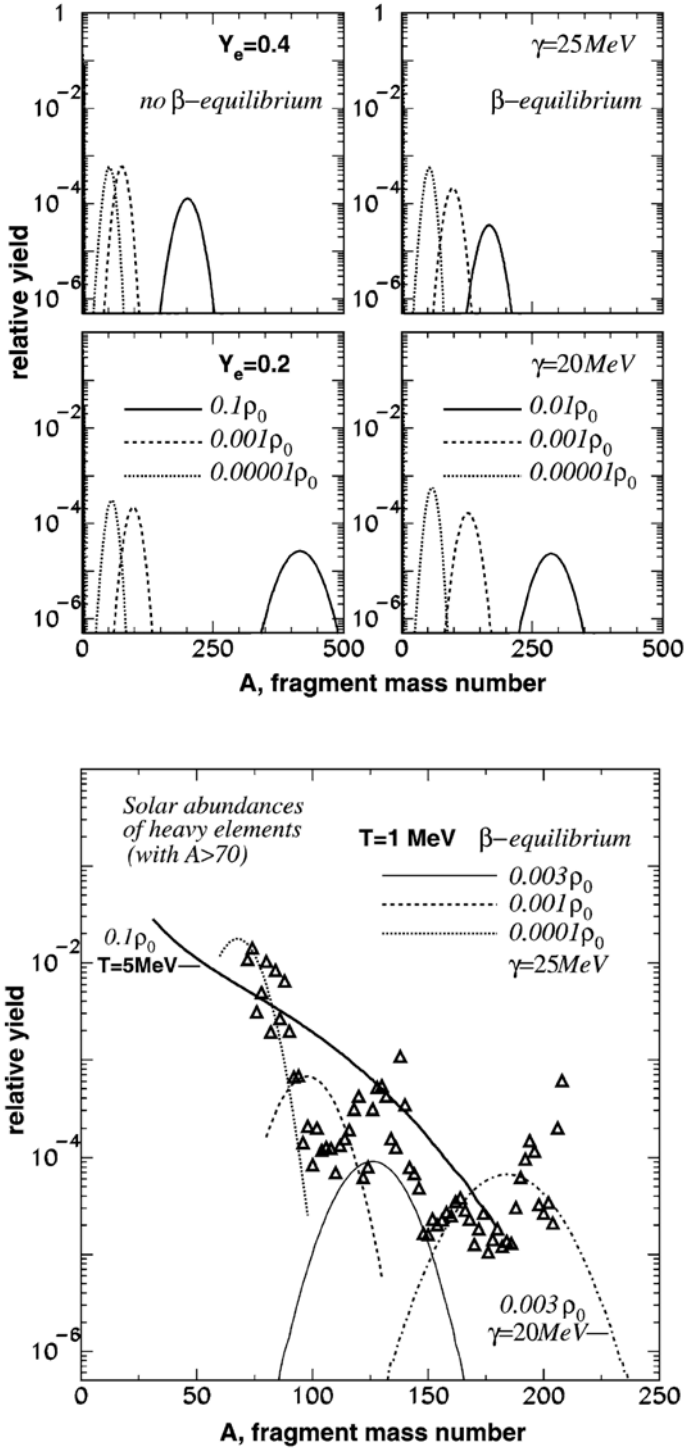

FIG. 7. Solar abundance of heavy elements as calculated from statistical model of multifragmentation for various values of the symmetry energy [7].

EXPERIMENT

A. Experimental Setup

The experiments were conducted at the Cyclotron Institute of Texas A&M University (TAMU) using the K500 Superconducting Cyclotron and the K1200 Cyclotron of the National Superconducting Cyclotron Laboratory (NSCL) at Michigan State University. Targets of ^{58}Fe (2.3 mg/cm^2) and ^{58}Ni (1.75 mg/cm^2) were bombarded at 33 and 45 MeV/nucleon for the TAMU measurement [35] and 25 and 53 MeV/nucleon for the NSCL measurements [36]. The different target and beam combinations result in composite systems with a total mass of A=98 and a range of neutron-to-proton ratio of N/Z=1.04 to 1.23.

The TAMU experiment used electron deficient ^{40}Ca and ^{40}Ar beams. The electrons were removed by passing the beam through a thin foil, and the resulting beam was then focused onto the center of the target inside the TAMU 4π neutron ball [37]. The light charged particles ($Z\leq2$) and intermediate mass fragments (IMFs) ($Z>2$) were detected inside the scattering chamber using six telescopes each consisting of a gas ionization chamber (IC) followed by a successive pair of silicon strip detectors (Si-Si) then either a single cesium iodide (CsI(T1)) scintillator crystal or a two CsI(T1) crystals side by side read out by a photodiode. This combination provided three distinct detector pairs (IC-Si, Si-Si, and Si-CsI) for fragment identification. The detector telescopes were set up at laboratory angles of 11, 44, 72, 100, 128, and 148 degrees. A schematic

diagram of the setup is shown in figure 8. The IC was of axial field design and filled with CF_4 gas at a pressure of 50 Torr. The 6cm thick gas-ionization chamber had a threshold of ~ 0.5 MeV/nucleon for intermediate mass fragments. The silicon detectors had an active area of 5cm x 5cm segmented into 4 quadrants allowing for two different angles to be studied with one telescope. The silicon detectors were 0.14 mm and 1 mm thick, respectively and had a dynamic range of ~16-50 MeV for ^{4}He and ~90-270 MeV for ^{12}C. The silicon pairs were followed by a 2.54cm thick CsI crystal read out by photodiodes. Good elemental (Z) identification was achieved for fragments that punched thought the IC detector and stopped in the first silicon detector. Fragments measured in the Si-Si detector pair also had good isotopic separation. Fragments that stopped in the CsI detectors showed isotopic resolution up to Z=7. The trigger for the data acquisition was generated by requiring a valid hit in one of the two silicon detectors.

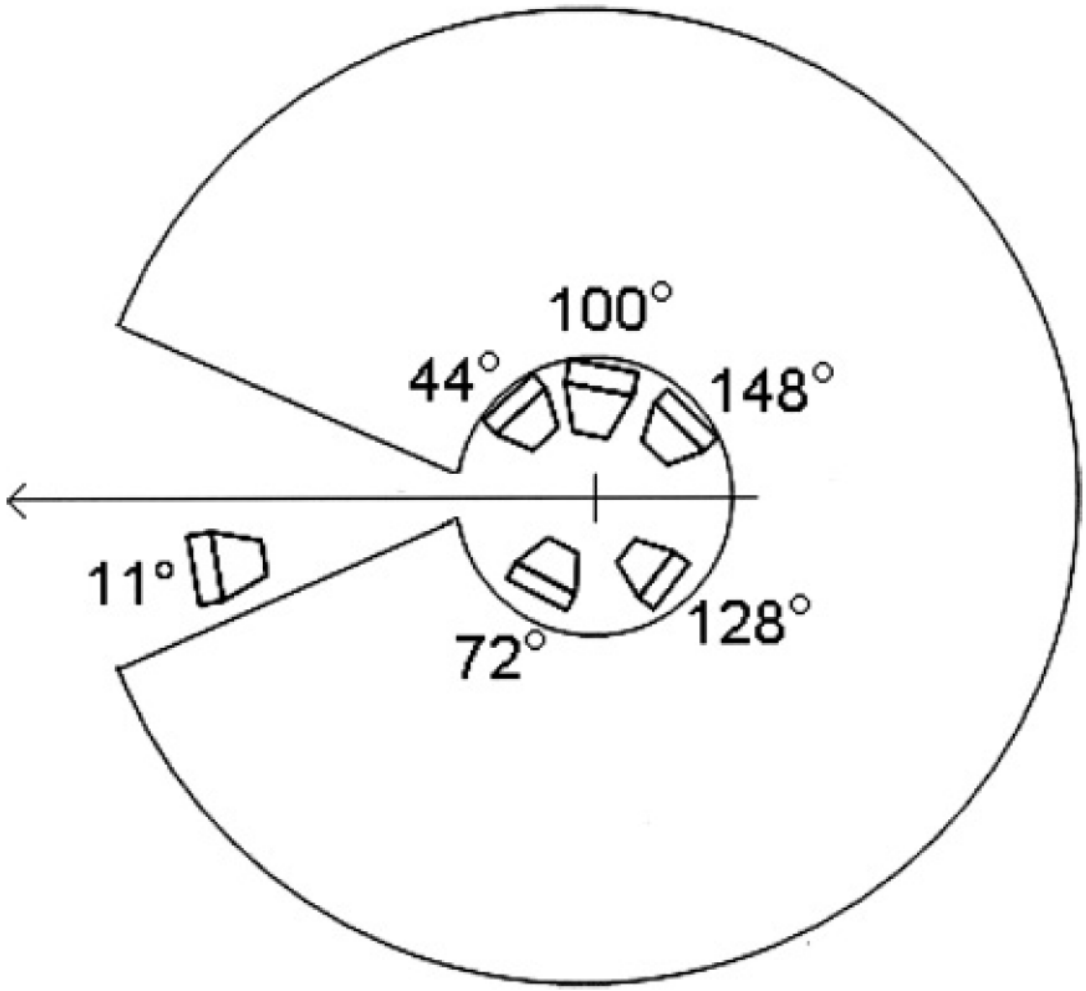

FIG. 8. Schematic diagram of the TAMU experimental setup showing the neutron ball with six telescopes [35].

The same reactions, $^{40}Ca+^{58}Ni$, $^{40}Ar+^{58}Ni$, and $^{40}Ar+^{58}Fe$, were measured in a 4π array at beam energies of 35 MeV and 50 MeV at the National Superconducting Cyclotron Laboratory (NSCL) at Michigan State University. The setup for the NSCL experiment consisted of 13 silicon detector telescopes placed inside the MSU 4π Array. Four telescopes were placed at 14°, each of which consisted of 100-μm-thick and 1-mm-thick silicon surface-barrier detector followed by a 20-cm-thick plastic scintillator. Five telescopes were placed at 40°, in front of the most forward detectors in the main ball of the 4π Array. They each consisted of 100-μm surface-barrier detector followed by a 5-mm lithium drifted silicon detector. More details can be found in Ref. [36]. Good isotopic resolution was obtained as in TAMU measurements.

B. Calibration

The calibration of the IC-Si detectors were carried out using the standard α source and by operating the IC at various gas pressures. The Si-Si detectors were calibrated by measuring the energy deposited by the α particles in the thin silicon and the punch-through energies of the different isotopes in the thick silicon. The Si-CsI detectors were calibrated by selecting points along the different light charged isotopes and determining the energy deposited in the CsI crystal from the energy loss in the calibrated Si detector.

C. Event Characterization

The event characterization of the NSCL data was accomplished by detection of nearly all the coincident charged particles by the MSU 4π Array. Data were acquired using two different triggers, the bulk of which were obtained with the requirement of the valid event in one of the silicon telescopes. Additional data were taken with a minimum bias 4π Array trigger for normalization of the event characterization. The impact parameter of the event was determined from the midrapidity charge detected in the 4π Array as discussed in Ref. [38]. The effectiveness of the centrality cuts was tested by comparing the multiplicity of the events from a minimum bias trigger with the multiplicity distribution when a valid fragment was detected at 40° [39]. The minimum bias trigger had a peak multiplicity of charged particles of one, whereas with the requirement of a fragment at 40°, the peak of the multiplicity distribution increased to 5.

The event characterization for the TAMU data was accomplished by using the 4π neutron ball that surrounded the detector assembly. The neutron ball consisted of 11 scintillator tanks segmented in its median plane and surrounding the vacuum chamber. The upper and the lower tanks were 1.5-m-diameter hemispheres. Nine wedge-shaped detectors were sandwiched between the hemispheres. All the wedges subtended 40° in the horizontal plane. The neutron ball was filled with a pseudocumene-based liquid scintillator mixed with 0.3 weight percentage of Gd salt (Gd 2-ethyl hexanoate). Scintillations from thermal neutrons captured by Gd were detected by twenty 5-inch phototubes (five in each hemisphere, one on each of the identical 40° wedges and two on

the forward edges). The efficiency with which the neutrons could be detected is about 83%, as measured with a ^{252}Cf source.

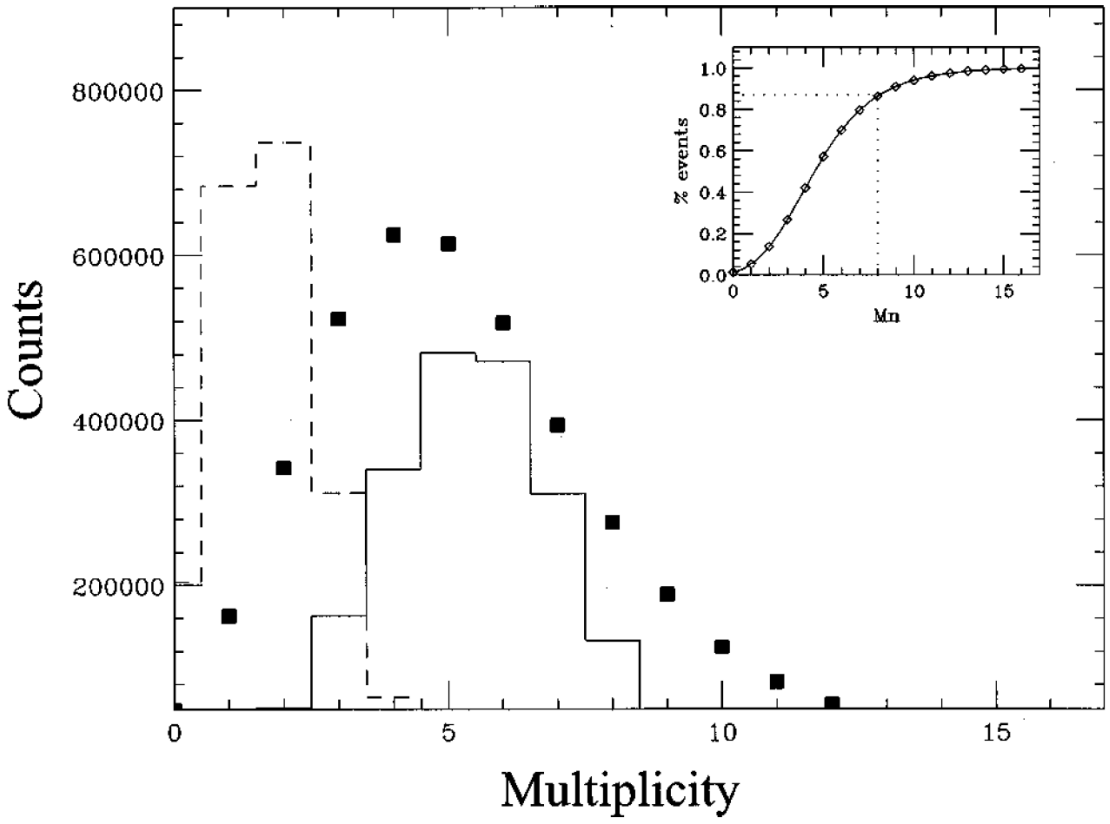

FIG. 9. Comparison between the experimental neutron multiplicity distribution and those predicted by BUU/GEMINI at impact parameters of b=0 and b=5. Neutron multiplicity distribution for the ^{40}Ar+^{58}Ni at 33MeV/nucleon, evaluated with BUU/GEMINI at b=0 (solid histogram) and b=5 (dashed histogram) and the experimental neutron multiplicity distribution (solid squares) [7].

The detected neutrons were used to differentiate between the central and peripheral collisions. To understand the effectiveness of neutron multiplicity as a centrality trigger, simulations were carried out using hybrid BUU/GEMINI calculations at various impact parameters for the $^{40}Ca+^{58}Fe$ reaction at 33 MeV/nucleon. Figure 9 shows the simulated neutron multiplicity distribution was compared with the experimentally measured distribution. The solid and the dashed histograms are the simulations for the b=0 and the b=5 impact parameters, respectively, were obtained using the BUU/GEMINI calculations. The multiplicity of neutrons for the impact parameter b=0 fm (solid histogram) collisions was found to be higher than the b=5 fm (dashed histogram) collision distribution. Once the impact parameter had been identified, gating on the highest 10% neutron multiplicity maximized the selection of central collisions.

To determine the contributions from the noncentral impact parameter collisions, neutrons emitted in coincidence with fragments at 40° and 152° from a hybrid calculation of BUU/GEMINI at b=0 and b=5 fm were analyzed. To adjust for geometrical cross section difference a ratio of b=0 to b=5 fm was made using the number of events with a neutron multiplicity of six or greater. These ratios were determined to be 19.0 and 11.1 at 40° and 1.3 and 2.2 at 152° at beam energies of 33 and 45 MeV/nucleon respectively. Intermediate angle ratios were not used due to the lack of events greater than six for the impact parameter b=5. Events were also filtered for detector acceptance and to further eliminate any possible target source contamination a cut of the highest 10% neutron event multiplicity was made.

In addition to the neutron multiplicity distribution, the charge distribution of the fragments was also used to investigate the contributions from central and mid-impact parameter collisions. The b=5 collisions produced essentially no fragments with charge greater than three in the 44° telescope.

To account for the central events of beam energies 25 and 53 MeV, earlier work [35] has proven that a lab angle of 44° maximizes the emission of primarily a primary composite source while it minimizes the target-like source and intermediate mass fragments keeping the equilibrium statistical model valid. This was done by determining the kinetic energy and charge distribution.

EXPERIMENTAL RESULTS

A. Relative Fragment Yield

The experimentally measured relative isotopic yield distribution for the lithium, beryllium and carbon element in $^{40}Ca+^{58}Ni$ (star symbols), $^{40}Ar+^{58}Ni$ (circle symbols), and $^{40}Ar+^{s58}Fe$ (square symbols), are shown in figure 10 for the beam energies of 25, 33, and 45 MeV/nucleon. The distribution for each element show a higher fragment yield for the neutron-rich isotopes in $^{40}Ar+^{58}Fe$ reaction (squares), which has the largest neutron-to-proton ratio (*N/Z*), in comparison to the $^{40}Ca+^{58}Ni$ (stars), which has the smallest neutron-to-proton ratio. The yields for the reaction $^{40}Ar+^{58}Ni$ (circles), which has an intermediate value of the neutron-to-proton ratio, are between those of the other two reactions. The figure thus shows the isospin dependence of the composite system on the properties of the fragments produced in the multifragmentation reaction. One also observes that the relative difference in the yield distribution between the three reactions decrease with increasing beam energy. This is due to the secondary deexcitation of the primary fragments, a process that becomes important for systems with increasing neutron-to-proton ratio and excitation energy. In the following subsections, we utilize the experimentally determined isotopic yield distributions to establish the isoscaling properties of the produced fragments before comparing them with the statistical multifragmentation model.

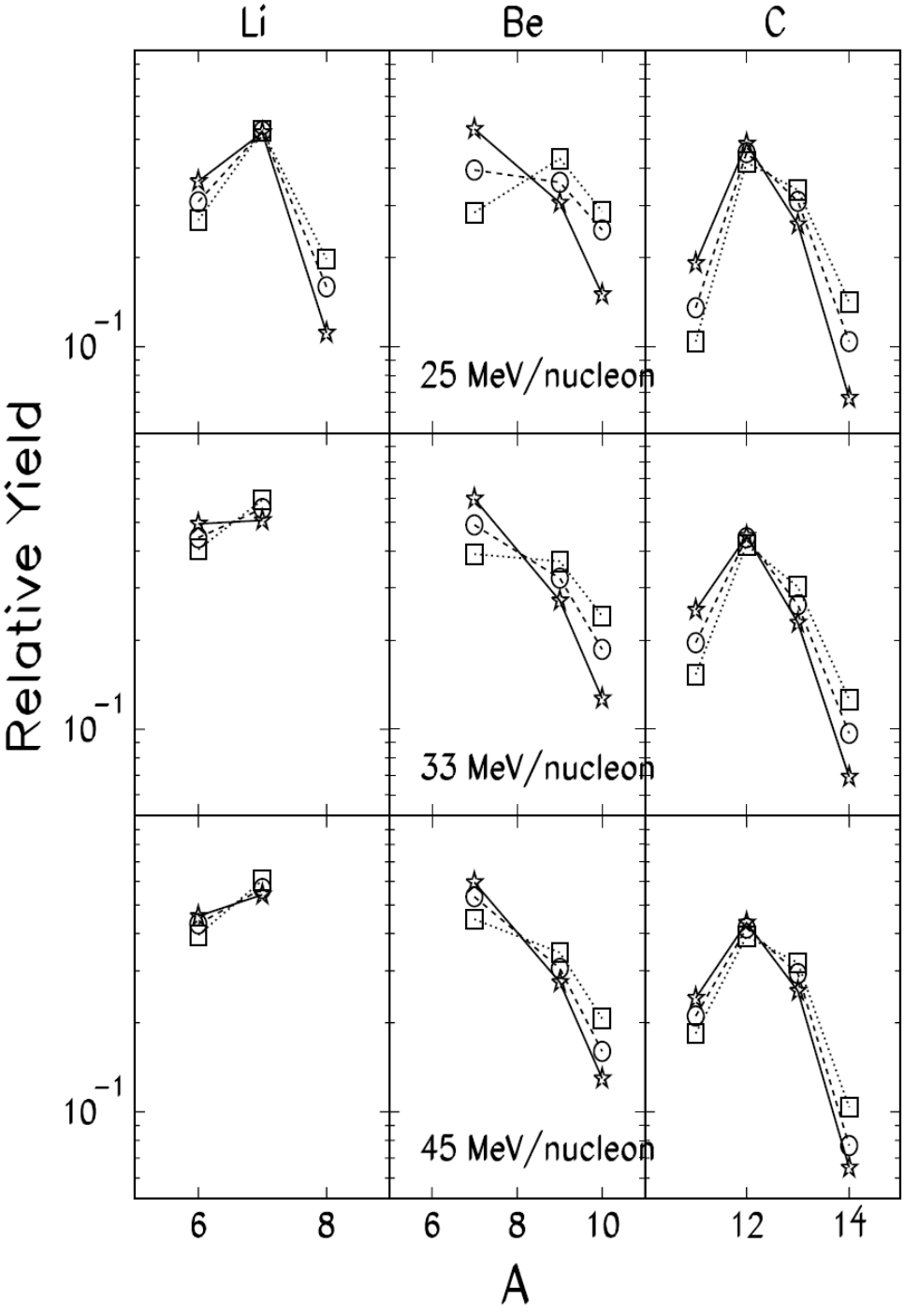

FIG. 10. Experimental relative isotopic yield distributions. The yeild for Lithium (left), Beryllium (center) and Carbon (right) for the beam energies of 25, 33, and 45 MeV/nucleon. The systems are represented as follows: ^{40}Ar+^{58}Fe (squares and dotted lines), ^{40}Ca+^{58}Ni (stars and solid lines), and ^{40}Ar+^{58}Ni (circles and dashed lines).

B. Isotopic and Isotonic Yield Ratios

To better explore the symmetry energy term of the nuclear equation of state, the isospin dependence and its effects must be understood. These can be studied by comparing systems of similar mass and temperature but differing in isospin asymmetry. In a multifragmentation reaction, the ratio of isotope yields in two different systems, 1 and 2, $R_{21}(N,Z) = Y_2(N,Z)/ Y_1(N,Z)$, has been shown to obey an exponential dependence on the neutron number (N) and the proton number (Z) of the isotopes, an observation known as isoscaling [8,40-42]. The dependence is characterized by a simple relation,

$$R_{21}(N,Z) = Y_2(N,Z)/Y_1(N,Z) = Ce^{N\alpha+Z\beta}, \tag{2.1}$$

where $Y_2(N,Z)$ and $Y_1(N,Z)$ are the yields from the neutron-rich and neutron-deficient systems respectively. C represents the normalization constant and $\alpha = \Delta\mu_n / T$ and $\beta = \Delta\mu_p / T$ reflect the isoscaling parameters. The quantities $\Delta\mu_n$ and $\Delta\mu_p$ are, respectively, the difference in the neutron and proton chemical potential, and T is the temperature.

In figure 11 the relative yield ratio, $R_{21}(N,Z)$, for each energy and system are plotted as a function of the neutron number N and proton number Z. The characteristic linearization of each isotope and isotone display the isospin dependence of these systems which will be further discussed in the next section. For the qualitative analysis of α and

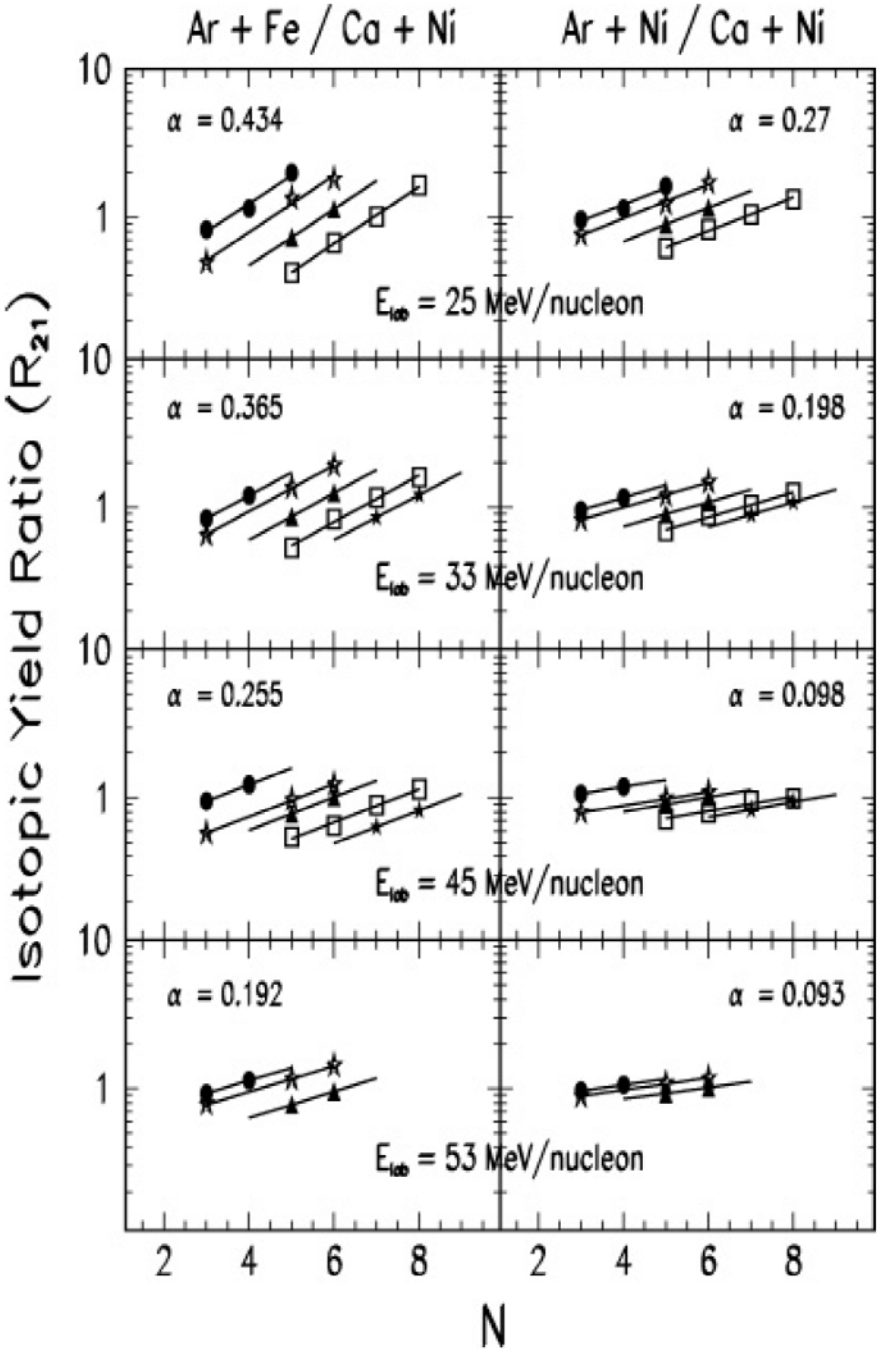

FIG. 11. Experimental isotopic yield ratios. The fragments as a function of neutron number N are shown and the left columns correspond to ^{40}Ar+^{58}Fe and ^{40}Ca+^{58}Ni reaction and the right columns correspond to ^{40}Ar+^{58}Ni and ^{40}Ca+^{58}Ni reaction with Z = 3 (circles), Z = 4 (open stars), Z = 5 (triangles), Z = 6 (squares), and Z=7 (filled stars).

β, exponential lines were fitted to the yield the fragments of each element (*Z*). The slopes of each beam energy were averaged resulting in an average α and β for each energy.

C. Double Isotope Ratio Temperature

The necessary condition for observing isoscaling in a multifragmentation reaction is the near equality of temperature for the systems of interest [43]. For the present work, this condition was tested by determining the temperature using the double isotope ratio method developed by Albergo *et al.* [44]. The Albergo method relates the apparent temperature, T of the system at the freeze-out density to the double isotope ratio, $R_{21}(N,Z) = Y_2(N,Z)/Y_1(N,Z) = Ce^{N\alpha+Z\beta}$. The modified version of the double isotope ratio assumes that the total angular momentum of the ground state fragments are the same for all systems reducing Eq. (2.1) to

$$R = \frac{Y(A_1,Z_1)\big/Y(A_1+1,Z_1)}{Y(A_2,Z_2)\big/Y(A_2+1,Z_2)} = \frac{e^{\Delta B/T}}{a}, \tag{2.2}$$

$$\Delta B = B(Z_1,A_1) - B(Z_1,A_1+1) - B(Z_2,A_2) + B(Z_2,A_2+1) \tag{2.3}$$

where $a \approx 1.59$ is a constant derived from ground state spin factors, T is the system freeze out temperature, and $B(Z, A)$ is the binding energy of a nucleus with the charge Z and the mass A. The resulting reduced equation relating the freeze out temperature to the double isotope ratio is

$$T = \frac{\Delta B}{\ln(aR)}. \tag{2.4}$$

This method was applied to all systems and beam energies studied. Figure 12 shows the double isotope ratios obtained using various combinations of isotopes as a function of the difference in binding energy. The top, middle, and bottom sections display the constant temperature that corresponds to the respective beam energies 25, 45, and 53 MeV/nucleon. The circles represent the ^{40}Ca+^{58}Ni reaction, squares the ^{40}Ar+^{58}Ni reaction, and triangles the ^{40}Ar+^{58}Fe reaction. A line was drawn to emphasize the constant temperature of the reactions at each beam energy. The resulting slope is the freeze out temperature at each beam energy, 5.8 MeV for 25 MeV/nucleon, 7.2 MeV for 45 MeV/nucleon and 9.0 MeV for 53 MeV/nucleon. An observation can be made that as the beam energy increases the temperature or excitation energy of the system also increases. The systems of interest are consistent with thermal equilibrium and illustrates this by the constant slope, or temperature, of the composite systems. Another observation is that the temperature increases as the energy of the system increases.

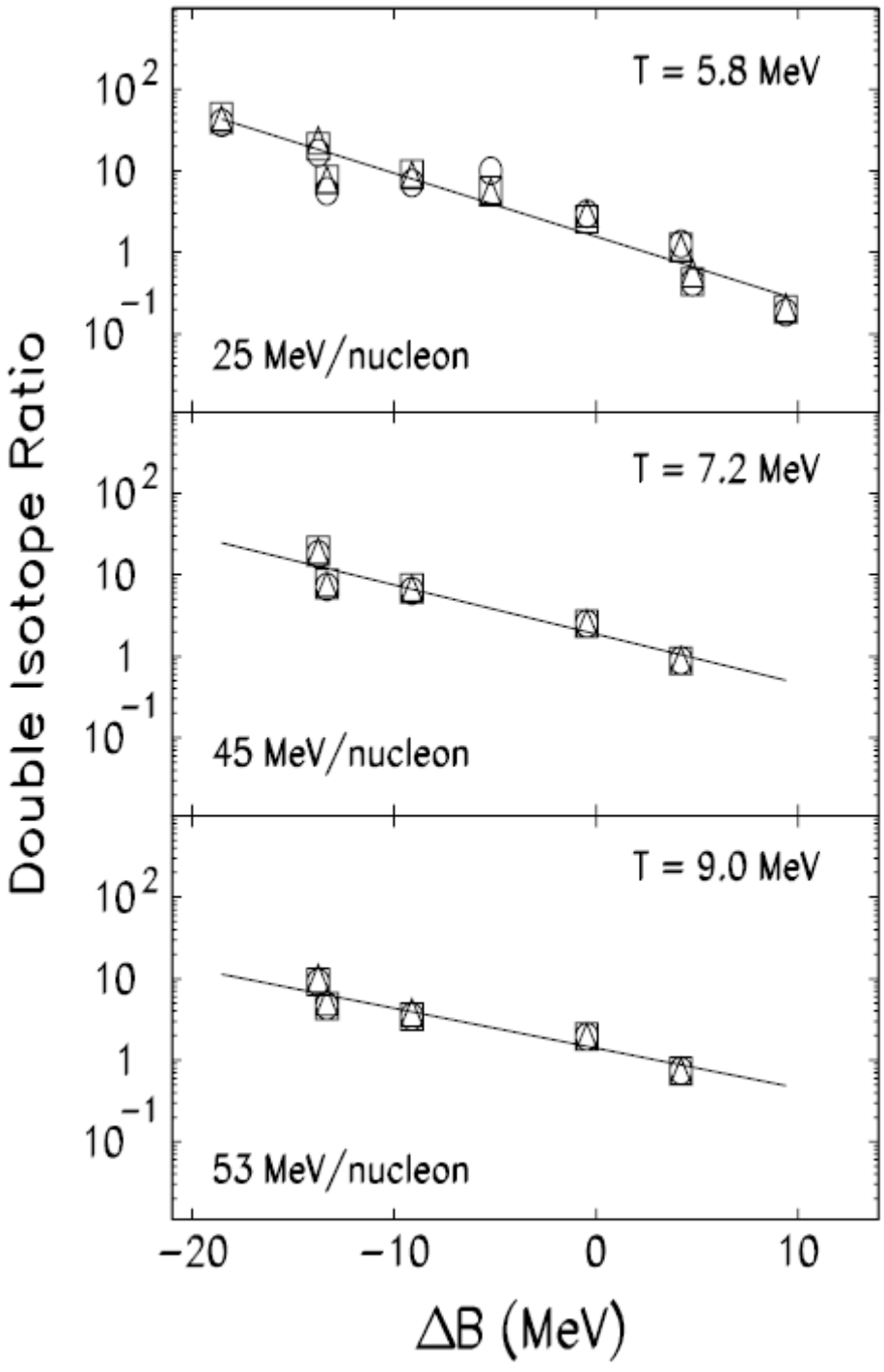

FIG. 12. Double isotope ratio temperatures corresponding to 25, 45, and 53 MeV/nucleon beam energies. The circles represent the ^{40}Ca+^{58}Ni reaction, squares the ^{40}Ar+^{58}Ni reaction, and triangles the ^{40}Ar+^{58}Fe reaction.

Figure 13 shows the relative comparison of how the α and β parameters react with different beam energies and isospin systems. Using the average α and β for each beam energy and reaction set, a decreasing α (increasing β) with an increase in beam energy is observed.

The neutron scaling parameter, *S(β,N)*, can also be calculated using the unique values of β from the isobaric yield ratios where

$$S(\beta, N) = R_{12}(N, Z)e^{-\beta Z}. \tag{2.5}$$

$S(\beta, N)$, is known to vary over a large range of data, from deep inelastic heavy ion collisions at low energies, through evaporation reactions induced by light and heavy ion projectiles to high energy heavy ion reactions characterized by intermediate mass fragments and multifragmentation. Figure 14 illustrates how *S(β,N)*, the scaled isotopes, lie very nicely along a straight line. *S*(β,*N*) for the two different isospin pairs is plotted as a function of neutron number *N* for beam energies of 25 and 45 MeV/nucleon. The figure also shows a significant difference in the scaling for the two beam energies, indicating a temperature influence on the isotopic yields.

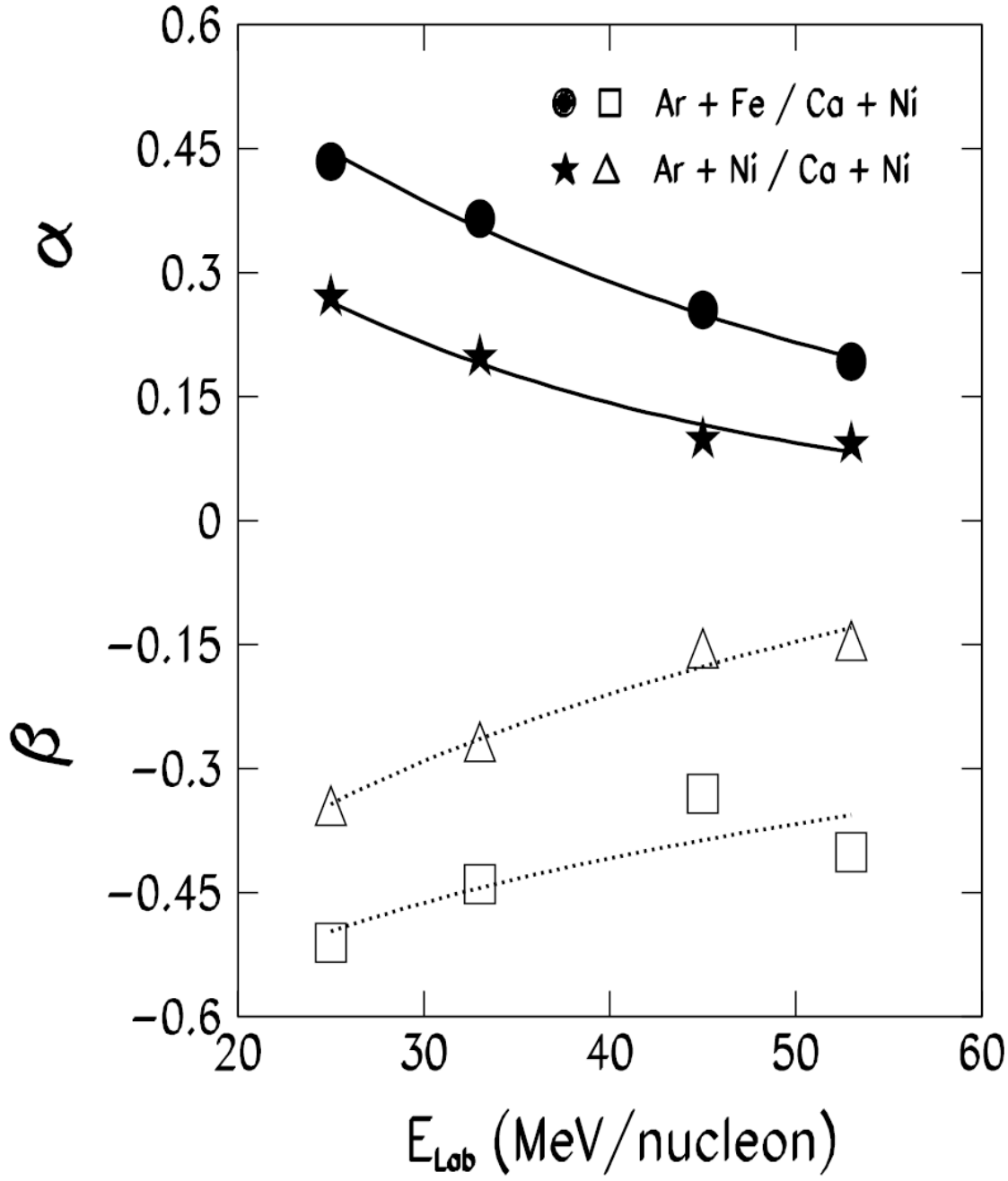

FIG. 13. Isoscaling parameters α (solid symbols) and β (open symbols) as a function of beam energy. This is shown for the ^{40}Ar+^{58}Fe/^{40}Ca+^{58}Ni and the ^{40}Ar+^{58}Ni/^{40}Ca+^{58}Ni reaction.

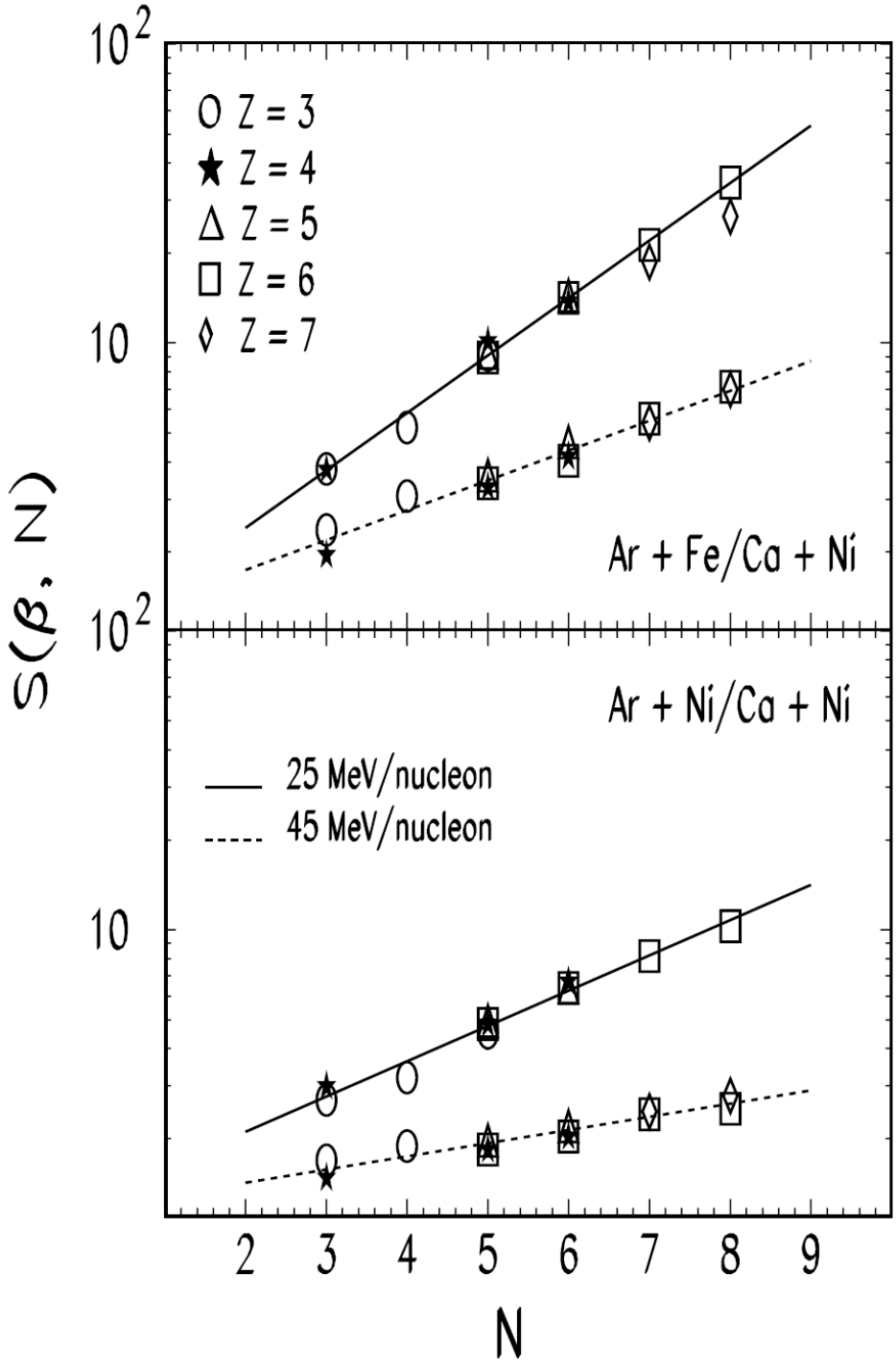

FIG. 14. The scaled isotope ratio S(β), as a function of the neutron number *N*. This is shown for different elements ($3 \leq Z \leq 7$) and different beam energies (25 and 45 MeV/nucleon). The top panel is for the $^{40}Ar+^{58}Fe/^{40}Ca+^{58}Ni$ reaction pair and the bottom panel shows the $^{40}Ar+^{58}Ni/^{40}Ca+^{58}Ni$ reaction.

D. Reduced Neutron and Proton Densities

In the Grand-Canonical approach of multifragmentation [44-47], the fragment yield distribution can be used to extract the reduced neutron and proton densities. The fragment yield $Y(N,Z)$ can be written as:

$$Y(N,Z) \propto V\rho_n^N \rho_p^Z Z_{N,Z}(T) A^{3/2} e^{B(N,Z)/T}, \tag{2.6}$$

where V is the volume of the system, $\rho_n \propto e^{\mu_n/T}$ and $\rho_p \propto e^{\mu_p/T}$ are the primary "free" neutron and proton densities, respectively. μ_n and μ_p are the neutron and proton chemical potentials. $Z_{N,Z}(T)$ is the intrinsic partition function of the excited fragment with temperature T and ground state binding energy $B(N,Z)$. The isotopic yield distribution of the fragments in terms of relative reduced neutron density is given as,

$$\frac{Y(N+k,Z)/Y^{Ca+Ni}(N+k,Z)}{Y(N,Z)/Y^{Ca+Ni}(N,Z)} = \left(\frac{\rho_n}{\rho_n^{Ca+Ni}}\right)^k, \tag{2.7}$$

where k represents different neutron numbers of the isotopes used to determine the double isotope ratio and Y_{Ca+Ni} is the yield for the ^{40}Ca+^{58}Ni reaction for which all particles are compared to in this work. Relative proton densities can be obtained by arranging the double ratios in the form,

$$\frac{Y(N,Z+k)/Y^{Ca+Ni}(N,Z+k)}{Y(N,Z)/Y^{Ca+Ni}(N,Z)} = \left(\frac{\rho_p}{\rho_p^{Ca+Ni}}\right)^k . \quad (2.8)$$

By relating the primary "free" neutron and proton densities, $\rho_n \propto e^{\mu_n/T}$ and $\rho_p \propto e^{\mu_p/T}$, and where k represents different proton numbers of the isobars used to determine the double isotope ratio. With the secondary "free" neutron and proton densities of ^{40}Ca+^{58}Ni, the reduced density ratio can be written as,

$$\frac{\rho_n}{\rho_n^{Ca+Ni}} \propto \frac{e^{\mu_{n1}/T}}{e^{\mu_{n2}/T}} = e^{\alpha} \text{ and } \frac{\rho_p}{\rho_p^{Ca+Ni}} \propto \frac{e^{\mu_{p1}/T}}{e^{\mu_{p2}/T}} = e^{\beta} , \quad (2.9)$$

where $\alpha = \Delta\mu_n / T$ and $\beta = \Delta\mu_p / T$, the difference in chemical potential divided by the temperature.

The top panel in figure 15 compares the relative free neutron density to the change in *N*/*Z* of the systems, ^{40}Ca+^{58}Ni (circles), ^{40}Ar+^{58}Ni (squares) and ^{40}Ar+^{58}Fe (triangles) reactions, at various beam energies. For a given change in *N/Z*, an increase in beam energy produces a decrease in the reduced neutron density. Overall, as the change in *N/Z* increases so does the reduced neutron density. The bottom panel shows how the reduced proton densities decrease as Δ(N/Z) increase and for a given change in N/Z, the relative proton density decrease as the beam energy increase. The asymmetry is found to decrease from ~ 1.0 at 25 MeV/nucleon to ~0.6 at 45 MeV/nucleon for the Ar+Fe/Ca+Ni reaction pair. The observed decrease in the relative neutron and proton densities with

increasing beam energy is attributed to the decrease in the sensitivity of the isospin effect with increasing temperature.

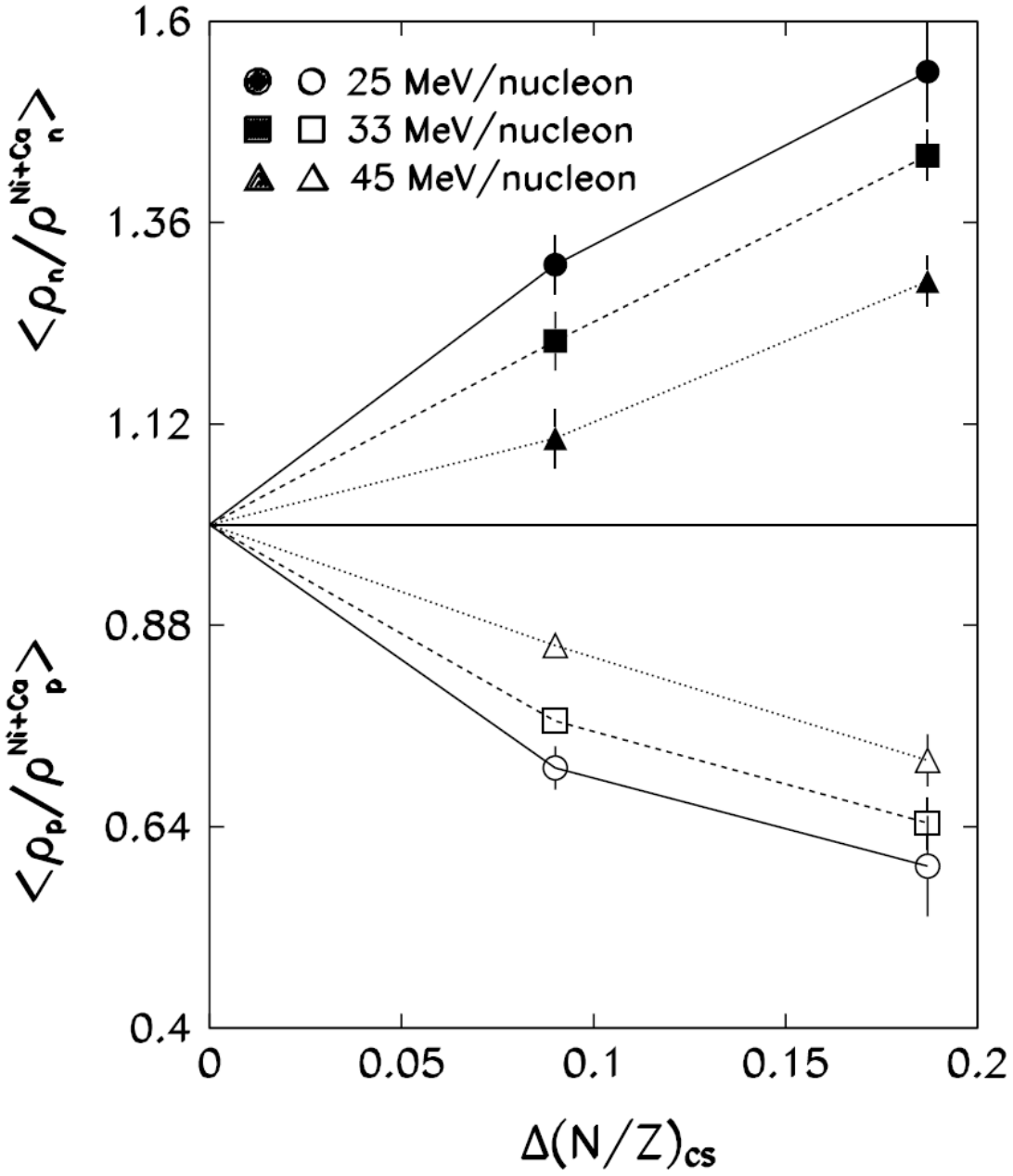

FIG. 15. Reduced densities of free neutrons (solid symbols) and protons (hollow symbols) at energies of 25, 33 and 45 MeV/nucleon. The circles represent ^{40}Ca+^{58}Ni reaction, squares the ^{40}Ar+^{58}Ni reaction, and triangles the ^{40}Ar+^{58}Fe reaction.

THEORETICAL CALCULATIONS

A. Statistical Multifragmentation Model

Statistical modeling [45-50] is often used to describe the multifragmentation [51-57] of a highly excited system, which is also believed to be related to the liquid-gas phase coexistence in low density expanding nuclear matter. (When a system becomes excited to the point that fragmentation is the preferred method of stabilization, the energy of the system becomes a very important aspect in choosing a statistical modeling method.) For systems of excitation energy $E^{*}<2$ MeV/nucleon it is plausible for evaporation to occur. This consists of small particle emissions, particles no larger than α-particles, with thermal equilibrium occurring between these emissions, but the systems of interest are significantly above the designated $E^{*}=3$MeV/nucleon. To better simulate how higher excitation energy systems behave the Statistical Multifragmentation Method (SMM) [45,58] is able to describes the evolution from sequential decay to a simultaneous break-up at a freeze-out volume. The freeze-out volume describes the phase space (spatial and momentum) factors at which a system has stopped all collisions and all the fragments are trapped within the local mean field just before multifragmentation. SMM also has the ability to describe the liquid-gas phase transition and has predicted distinctive features, such as the plateau like region in a caloric curve.

SMM is based on the assumption of a simultaneous break-up of a thermalized nuclear system. Using a microcanonical approach and Monte Carlo sampling, this

model takes into account the effects of nuclear features such as finite size effects, internal excitation of fragments, and strong Coulomb interactions between the fragments which are treated in the Wigner-Seitz approximation. Light fragments, with $A \leq 4$, are treated as elementary particles with only transitional degrees of freedom ("nuclear gas"), while fragments, with $A > 4$, are treated as heated nuclear liquid drops. The hot fragments in SMM undergo a de-excitation process via evaporation and Fermi break-up. The individual free energies, $F_{A,Z}$, are parameterized as a sum of the volume, surface, Coulomb, and symmetry energy,

$$F_{A,Z} = E^{V}_{A,Z} + E^{S}_{A,Z} + E^{C}_{A,Z} + E^{sym}_{A,Z} \tag{3.1}$$

where the volume energy is represented by the equation:

$$E^{V}_{A,Z} = (W_0 - T^2 / \varepsilon_0) A \,. \tag{3.2}$$

with parameter ε_0 is related to the level density and $W_0 = 16\,\mathrm{MeV}$ is the binding energy of infinite nuclear matter. The surface energy is represented by the equation:

$$E^{S}_{A,Z} = B_0 A^{2/3} [(T_c^2 - T^2)/(T_c^2 + T^2)]^{5/4}, \tag{3.3}$$

with, $B_0 = 18\,\mathrm{MeV}$ being the surface coefficient and $T_c = 18\,\mathrm{MeV}$ being the critical temperature of infinite nuclear matter. The Coulomb energy is represented by the equation:

$$E_{A,Z}^{C} = cZ^2 / A^{1/3}, \tag{3.4}$$

where, $c = (3/5)(e^2 / r_0)[1-(\rho/\rho_0)^{1/3}]$, is the Coulomb parameter obtained in the Wigner-Seitz approximation with charge unit e, and $r_0 = 1.17\,\mathrm{fm}$. The symmetric energy is represented by the equation:

$$E_{A,Z}^{sym} = \gamma(A-2Z)^2 / A, \tag{3.5}$$

where, $\gamma = 25\,\mathrm{MeV}$ is the symmetry energy co-efficient. These parameters were acquired from the Bethe-Weizsacker mass formula and correspond to the assumption of isolated fragments with normal density in the freeze-out configuration [45,47]. Nuclear multifragmentation is characterized by increasing excitation energy and expanding systems. The isospin of the source also influences the fragment production through the symmetry energy. By comparing the experimentally determined fragment yield distribution with the SMM calculation, the parameters of hot nuclei under multifragmentation conditions, including the symmetry energy, can be extracted. In the

following, it will be shown how this information can be obtained from the isoscaling phenomena.

B. Isoscaling and Symmetry Energy Coefficient

Isotopic scaling or isoscaling arise naturally in statistical equilibrium models of multifragmentation. In these models the difference in the chemical potential of systems with different *N*/*Z* is directly related to the scaling parameter α. It has been shown that the isoscaling parameter α is proportional to the symmetry energy part of the fragment binding energy though a relation,

$$\alpha = -\Delta s_n / T \approx \frac{4\gamma}{T}\left[\left(\frac{Z_1}{A_1}\right)^2 - \left(\frac{Z_2}{A_2}\right)^2\right] \tag{3.6}$$

where, Z_1, A_1 and Z_2, A_2 are the charge and the mass numbers of the fragmenting systems, *T* is the temperature of the system and γ, the symmetry energy coefficient [8].

C. Secondary De-excitation Effect on Isoscaling Parameter

The above relationship was derived for fragments at the freeze-out stage and in order to relate γ or α of hot primary fragments, obtained from the above formula, to the

γ or α of cold secondary fragments the effects of secondary de-excitation must be taken into account. In SMM, the secondary de-excitation of large fragments with A>16 is described by Weisskopf-type evaporation and Bohr-Wheeler-type fission models. The decay of small fragments is treated with a Fermi-breakup model. Weisskopf-type evaporation relates the probability for the emission of a particle with energy ε by a compound nucleus with mass number A and excitation energy E_A^* to the cross section $\sigma(\varepsilon)$. The partial decay rate for the emission of a light charged particle with energy ε and orbital angular momentum l_β from a compound nucleus with excitation energy E_A^* rotating with angular momentum L contains the level density parameter. In the Fermi-breakup model, all ground and nucleon-stable excited states of light fragments are taken into account and the population probabilities of these states are calculated according to the available phase space where it identifies a particle by its generalized coordinates and momentum [47].

EXPERIMENT AND THEORY: A COMPARISON

To provide a theoretical comparison for the experimentally observed results, the primary and secondary fragment isotopic yield distributions were calculated from the SMM. The calculations were carried out for the ^{40}Ca+^{58}Ni, ^{40}Ar+^{58}Ni and ^{40}Ar+^{58}Fe reactions at various excitation energies. Multifragmentation effects are related to the different dynamical paths a system can take during a collision. A detailed understanding of these dynamics is imperative to calculate the excitation energy per nucleon of the initial system and is very difficult to calculate accurately. A range of values for the excitation energy per nucleon from E^* = 4-10 MeV/nucleon was assumed, and the excitation energy corresponding to the beam energy was verified by an independent calculation using BUU – GEMINI (see Table II in Ref. [35]) along with the systematic calorimetric measurements available in the literature for systems with mass A~100 [59]. The mass and charge of the initial system, was assumed to be those of the initial compound nucleus. This is consistent with the dynamical calculations of Li *et al*. [60]. In the present analysis, the Z/A of the source was estimated from a dynamical BNV calculation [61]. These results were obtained [4] at a time, around 50 fm/c, after the projectile fuses with the target nuclei and the quadrupole moment of the nucleon coordinate approaches zero. The observed change was about 3% lower than the initial Z/A of the system. However, this change depends on the time at which the dynamical code is terminated, and therefore no change in the initial BNV calculated Z/A was used in this analysis. To account for the possible uncertainty in the source size due to the loss

of nucleons during pre-equilibrium emission, the SMM calculations were also carried out for sources with 80% of the total mass. No significant change in the isospin characteristics under study was observed. The freeze-out density in the calculation was assumed to be 1/3 of the normal nuclear density and the symmetry energy coefficient γ was taken to be 25 MeV.

A. Relative Yield Distribution (primary and secondary)

The calculated primary and secondary fragment yield distributions for the carbon isotopes in $^{40}Ca+^{58}Ni$, $^{40}Ar+^{58}Ni$ and $^{40}Ar+^{58}Fe$ reactions at various excitation energies are as shown in figure 16. The characteristics of the hot primary fragment yield distribution, shown in the left column of the figure, change significantly after the secondary de-excitation. The isospin effects are very prominent in primary fragment yield distribution at each excitation energy for the three systems at each excitation energy. These are shown by the dashed, dotted, and solid lines in the left column. It is observed that the most neutron rich system has the highest relative yield for the neutron rich isotopes and the lowest yield for the neutron-deficient isotopes. This effect seems to decrease with increasing excitation energy. A similar feature is also observed in the secondary fragment distribution shown in the right column of the figure, though the effect is observed to be weakened significantly. Furthermore, the means of the distribution is also observed to decrease along with the width for the secondary fragments.

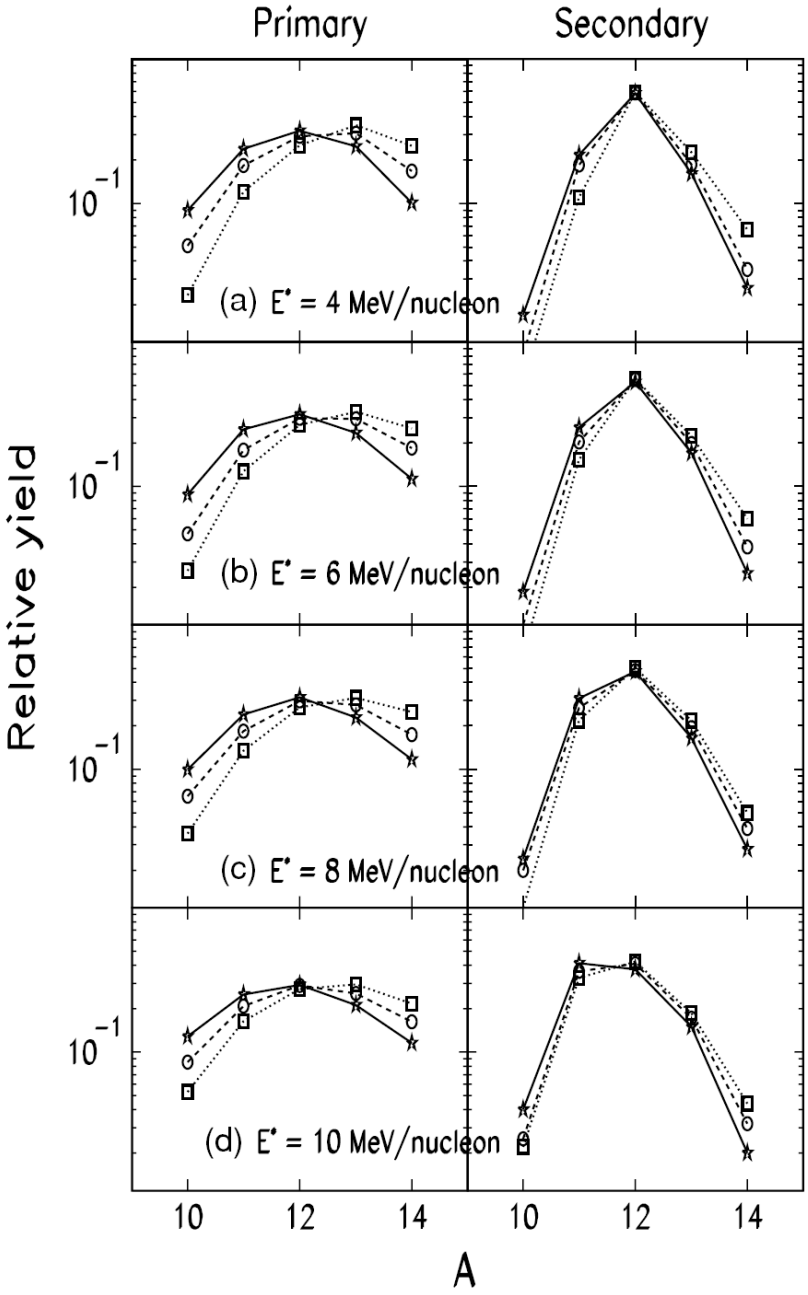

FIG. 16. Relative yield distribution of the primary (left) and secondary (right) fragments for the carbon isotope (Z=6) obtained from the SMM. The stars and solid lines represent ^{40}Ca+^{58}Ni reaction, circles and dashed lines represent ^{40}Ar+^{58}Ni reaction, and squares and dotted lines represent the ^{40}Ar+^{58}Fe reaction at various excitation energies. The symmetry energy assumed the SMM calculations γ = 25 MeV.

B. Isoscaling Parameter vs Excitation Energy

Qualitatively, the SMM simulates quite well the overall features of the experimentally observed isotopic yield distribution shown in figure 10. The isotopic yield ratios using the primary and secondary fragment distribution from the statistical multifragmentation model are show in figure 17 for the $^{40}Ca+^{58}Ni$ and $^{40}Ar+^{58}Ni$ reaction pair. It is observed that the yield ratios for both the primary and the secondary distribution obey the isoscaling relation quite well and adhere to the isoscaling phenomenon. There is also very little deviation in the α parameter between the primary and secondary fragments for a given excitation energy. Furthermore, the scaling parameter shows a gradual decrease as the excitation energy of the system increases, which is also observed in the experimental data (shown in figure 11).

Though the overall features of the scaling parameter calculated from the statistical multifragmentation model is reproduced quite well, the absolute values do not quite agree with the experimentally determined α. This is shown in the top panel of figure 18 where a comparison is made between the SMM calculated and experimentally observed values of α. In the figure, the left column corresponds to the $^{40}Ar+^{58}Ni$ and $^{40}Ca+^{58}Ni$ pair of reactions and the right to the $^{40}Ar+^{58}Ni$ and $^{40}Ca+^{58}Ni$ pair. The dotted

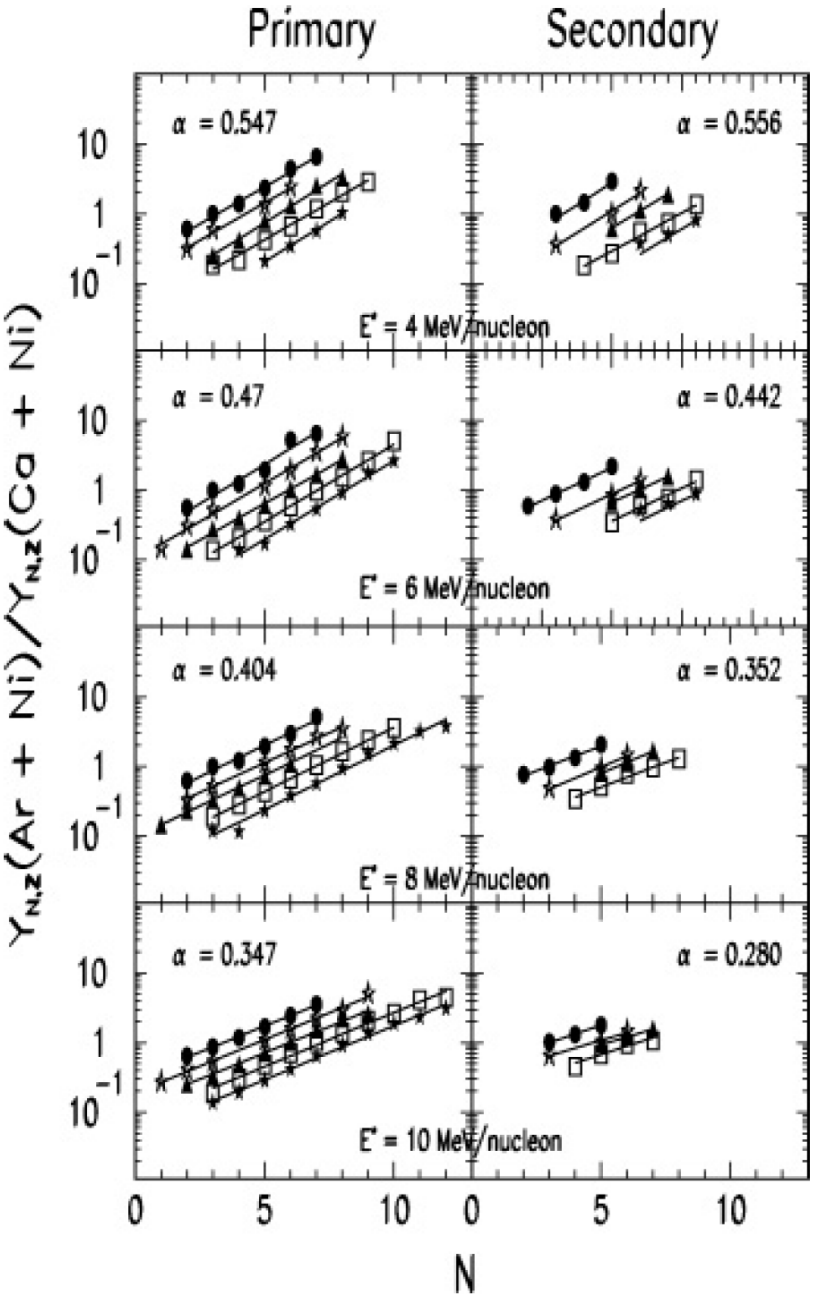

FIG. 17. Ratio of the calculated isotopic yield distributions for the systems. ^{40}Ar+^{58}Ni/^{40}Ca+^{58}Ni for the primary and secondary fragments along with the corresponding alpha for each excitation energy and the calculations are for a symmetry energy, γ = 25 MeV. The symbols for both systems correspond to Z=3 (circles), Z=4 (open stars), Z=5 (triangles), Z=6 (squares) and Z=7 (solid stars) elements.

line represents the primary fragments, the solid line represents the secondary fragments and the stars represent the calculated SMM isoscaling parameter for a given symmetry and excitation energy, and the symbols correspond to the experimentally determined alphas. It is observed that the experimentally determined alphas are significantly lower than the calculated values of α using the standard value of the symmetry energy. The dependence of the isoscaling parameter, α, on the excitation energy, and the symmetry energy of the hot primary fragment, γ, is illustrated in figure 18 when the γ in SMM was varied within the range 25-15 MeV and within an excitation energy range of E^*=4-10 MeV/nucleon. SMM was then run for different excitation and symmetry energies resulting in a collection of the corresponding isoscaling parameter, α. The first attempt, shown in the top panel of figure 18, was to simulate the traditional γ=25 MeV for the isolated cold nuclei in their ground state for each excitation energy, E^*. The second attempt, shown in the middle panel, was with γ=18 MeV at various excitation energies. At γ=18 MeV the simulated data started to agree a little closer with the experimentally determined data. The bottom panel shows the alpha calculated from SMM with γ=15 MeV. This resulted in the closest fit for both systems and all excitation energies. The experimentally determined α could be reproduced for both pair of systems at all excitation energies using a symmetry energy value of γ=15 MeV. This symmetry energy is significantly lower than the γ=25 MeV used for the ground state nuclei.

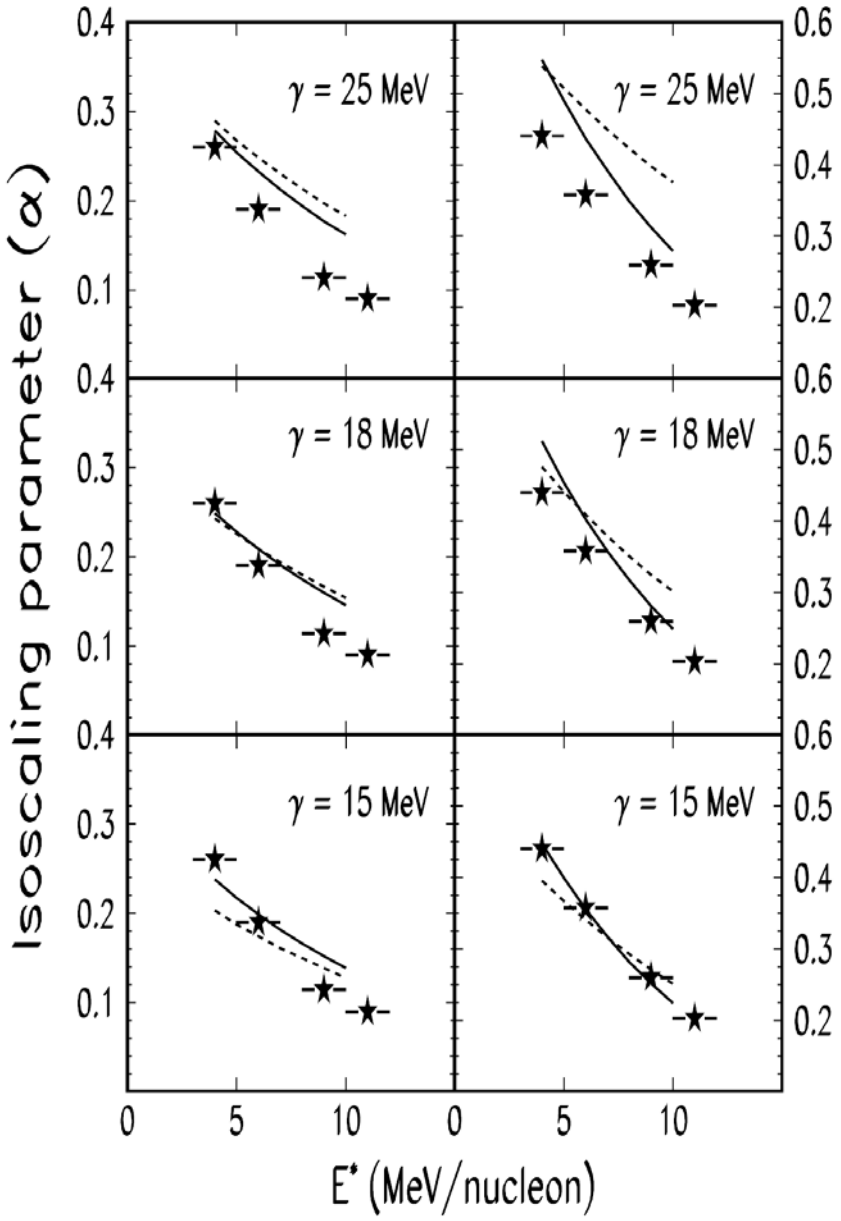

FIG. 18. Comparison of the SMM calculated isoscaling parameter, α, (lines) with the experimentally determined α (symbols) as a function of excitation energy for different values of the symmetry energy coefficient $\tilde{\gamma}$. The dotted lines correspond to the primary fragments and the solid lines correspond to the secondary fragments. The left column is the comparison for the ^{40}Ar+^{58}Ni/^{40}Ca+^{58}Ni system and the right column for the ^{40}Ar+^{58}Fe/^{40}Ca+^{58}Ni system.

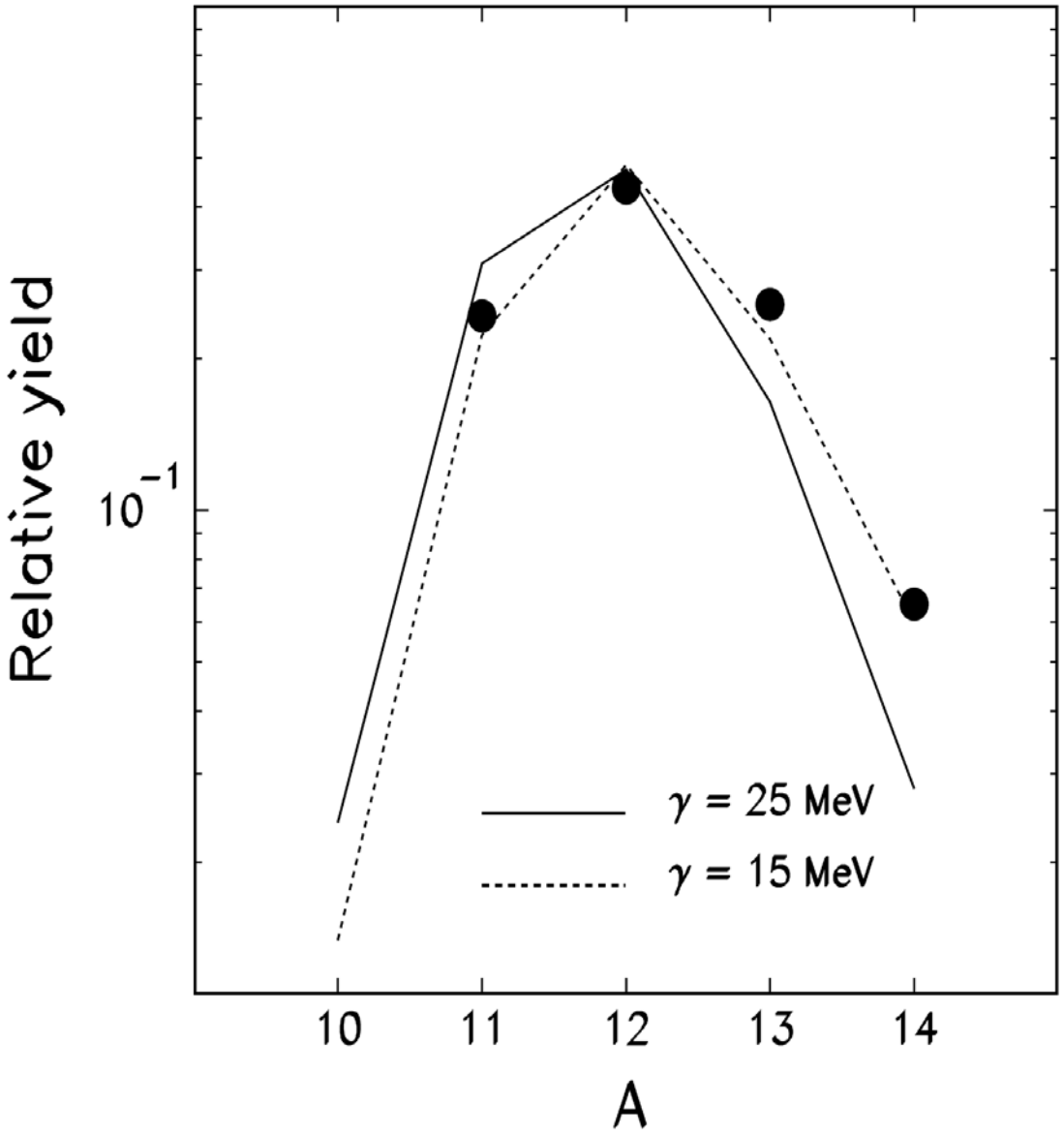

FIG. 19. SMM calculated ^{12}C isotopic yield distribution for various values of the symmetry energy, γ. The isotopic yield distribution is shown for the ^{40}Ca+^{58}Ni reaction at 45 MeV/nucleon. The solid line is the SMM calculation with symmetry energy coefficient γ=25 MeV, and the dashed line with γ=15 MeV. The solid points correspond to the experimental results.

In figure 19, a comparison between the experimentally determined carbon isotopic yield distribution (represented by solid dots) and the SMM calculated yield distribution, using two different values of the fragment symmetry energy at 15 MeV (dashed line) and 25 MeV (solid line) show a lower value of the symmetry energy, γ, is required to explain the experimental yield distribution. Due to the decrease in symmetry energy, the isotopic yield distribution results in more neutron rich fragments.

C. Isoscaling Parameter vs Symmetry Energy Coefficient

The calculated α is observed to decrease with decreasing symmetry energy, γ. The α values for the hot primary fragment (dotted lines) and the cold secondary (solid lines) fragment yield distributions for $^{40}Ar+^{58}Ni$ and $^{40}Ca+^{58}Ni$ reaction pair (the right column) and $^{40}Ar+^{58}Fe$ and $^{40}Ca+^{58}Ni$ reaction pair (the left column) for various excitation energies are shown in figure 20. The difference between the primary fragment α and the secondary fragment α is negligibly small for the Ar+Ni-Ca+Ni reaction pairs, which has the lower difference in neutron-to-proton ratio. The difference for the Ar+Fe-Ca+Ni pair, which has the higher neutron-to-proton ratio, is slightly larger at the highest excitation energies.

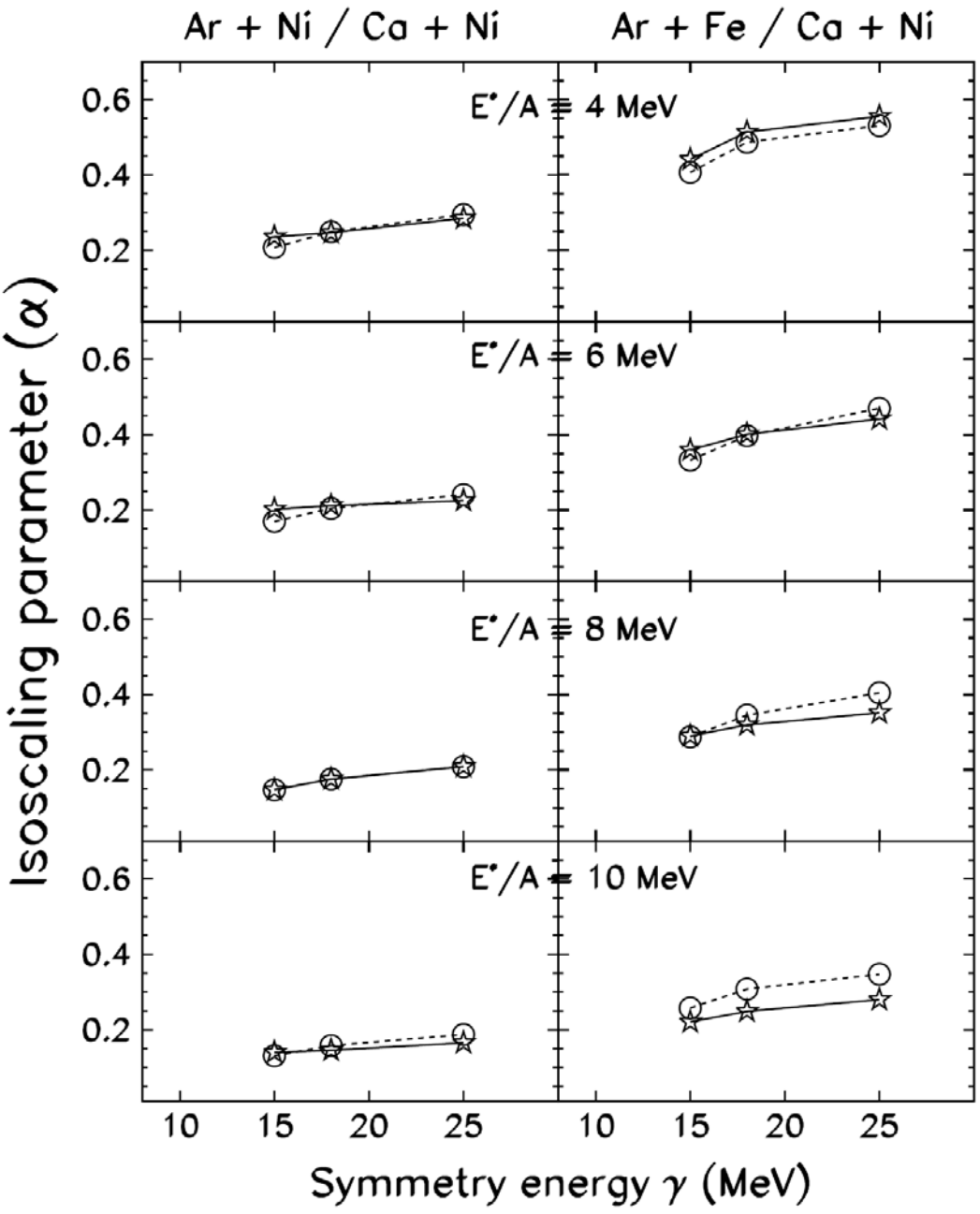

FIG. 20. SMM calculated isoscaling parameter α as a function of symmetry energy coefficient for various excitation energies. The open circles connected by dotted lines represent the primary fragments and the open stars connected by solid lines represent the secondary fragments. The right column shows the calculation for the ^{40}Ar+^{58}Fe/^{40}Ca+^{58}Ni system and the left column the ^{40}Ar+^{58}Ni/^{40}Ca+^{58}Ni system.

D. Isoscaling Parameter vs Excitation (with evolving mass)

A modified version of the previously discussed SMM calculation (which uses the standard mass of cold isolated nuclei) uses the mass of the hot fragments in the freeze-out configuration resulting an even smaller symmetry energy, γ. Fragments in their primary stage are usually hot and their properties (i.e., binding energies and masses) differ than those of cold nuclei. This configuration takes into account the effects of the symmetry energy evolution during the sequential de-excitation of the hot primary fragments. The mass of the hot fragments for $E^*/A > 1$ MeV was taken to be that of the liquid drop model,

$$m_{A,Z} = m_{ld}(\gamma) = m_n N + m_p Z - AW_o + \gamma \frac{(A-2Z)^2}{A} + B_o A^{2/3} + \frac{3e^2 Z^2}{5r_o A^{1/3}}, \qquad (26)$$

where $m_{ld}(\gamma)$ is the standard liquid-drop mass, m_n and m_p are the masses of the free neutrons and protons. The mass for $E^*/A \leq 1$ MeV was taken such that a smooth transition to standard experimental mass with shell effects could be described by the equation,

$$m_{A,Z} = m_{ld}(\gamma) * \xi + m_{\exp}(1-\xi). \qquad (27)$$

$m_{\exp}$ is the ground state mass and can be found from nuclear tables, and $\xi = \beta E^* / A$ where $\beta = 1$ MeV^{-1} and $x \leq 1$. The excitation energy, E^*, is determined from the energy balance equation taking into account the mass m_{AZ} at the given excitation [62]. The above corrections and the study of the effects of evolving mass during the sequential de-excitation of the hot primary fragments. Figure 21 shows the isoscaling parameter α plotted as a function of excitation energy for the two systems, Ar+Ni/Ca+Ni (left) and Ar+Fe/Ca+Ni (right) and shows the result of the modified secondary de-excitation correction. The top panels displays the primary (dotted lines) and secondary (solid lines) fragments using the cold isolated nuclei symmetry energy of γ=25MeV. As before, this modified calculation does not describe the experimental data sufficiently for either pair of systems. With decreasing values of the symmetry energy, shown in the lower panels of the figure, the calculated values of the isoscaling parameter, α, for the Ar+Ni and Ca+Ni (left column) reaction pair are in better agreement with the experimental values at the lower symmetry energy γ = 13 MeV. The calculated values for the Ar+Fe and Ca+Ni (right column) reaction pair is best described by the experimental values at γ = 10 MeV. In general, it can be observed that the modified version of the secondary de-excitation in SMM leads to a symmetry energy values between 10-13 MeV which is slightly lower than the previous standard SMM method of 15 MeV and much lower than the traditional 25 MeV.

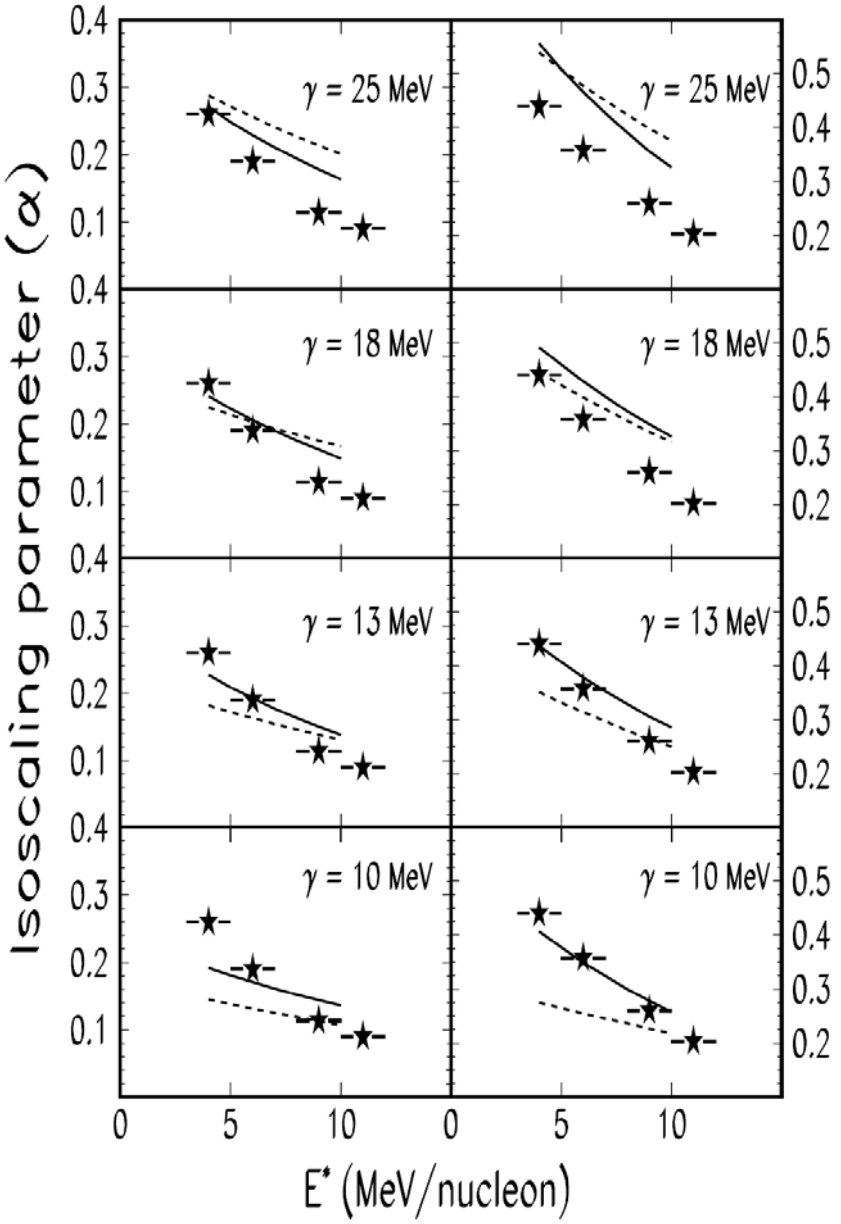

FIG. 21. Isoscaling parameter as a function of excitation energy calculated with the new sequential de-excitation mechanism. Comparison of the SMM calculated isoscaling parameter, α, (lines) with the experimentally determined α (symbols) as a function of excitation energy for different values of the symmetry energy coefficient γ. The dotted lines correspond to the primary fragments and the solid lines correspond to the secondary fragments. The left column is the comparison for the ^{40}Ar+^{58}Ni/^{40}Ca+^{58}Ni system and ^{40}Ar+^{58}Fe/^{40}Ca+^{58}Ni system is displayed in the right column.

The isoscaling parameter as a function of the symmetry energy for the primary and secondary fragments at various excitation energies is shown in figure 22. As seen in figure 20, the difference in α between the primary and secondary fragments is extremely small for the Ar+Ni / Ca+Ni (left column) reaction and slightly larger for the Ar+Fe / Ca+Ni (right column) reaction. This slight difference is due to the fact that the Ar+Fe / Ca+Ni reaction pair has a higher difference in neutron-to-proton ratio. However, the main difference between figure 20 and figure 22 is the rate at which the isoscaling parameter α decreases with decreasing symmetry energy. Using the modified secondary de-excitation with evolving symmetry energy, the decrease in α is much more gradual than the SMM calculation that does not take the symmetry energy dependence of the mass into account. This enables the calculation to reproduce the experimental α value with a slightly lower value of symmetry energy, γ =10-13 MeV. It can also be observed that at the lower symmetry energies of the primary fragment α is constantly smaller than the secondary fragment α at the same symmetry energy.

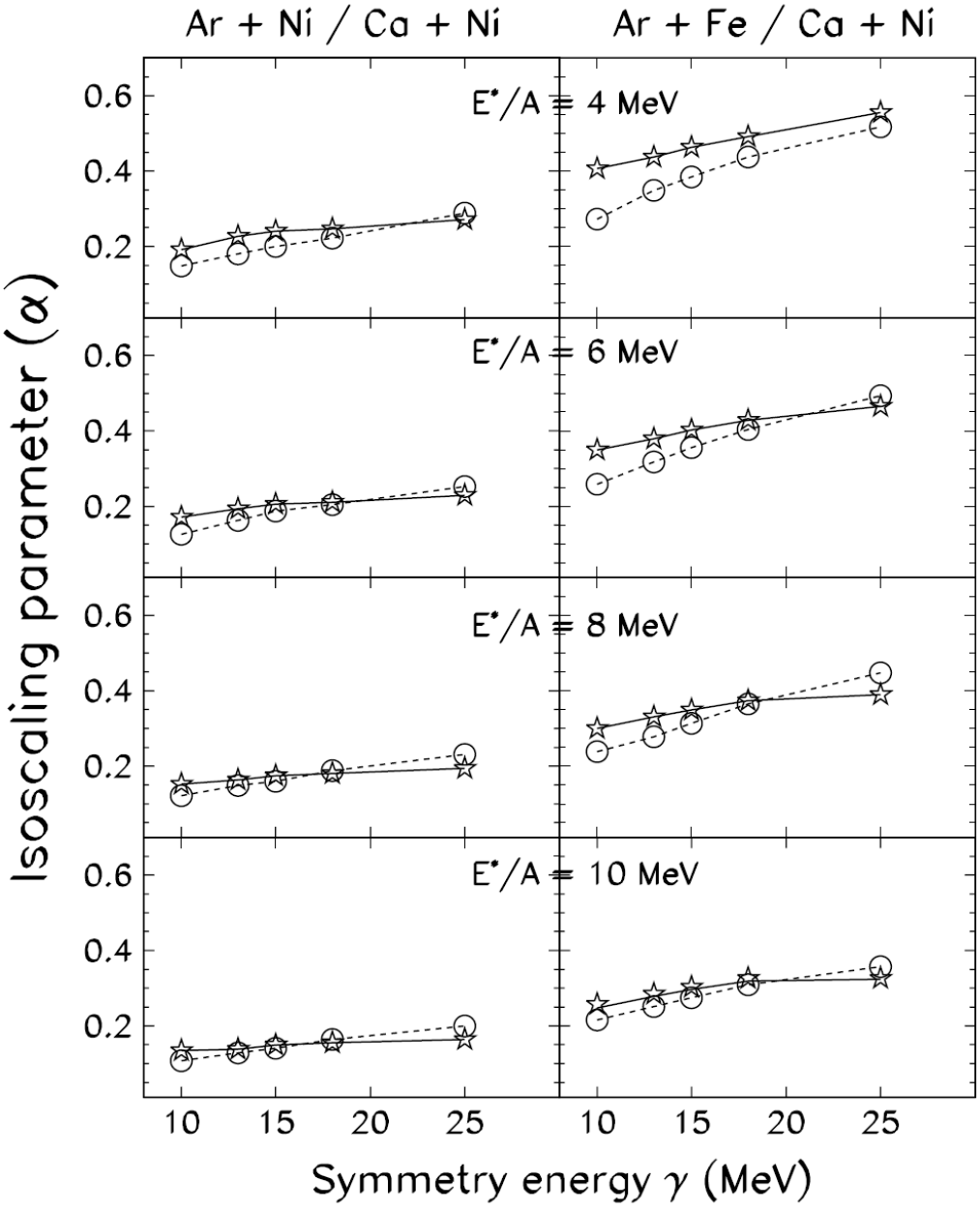

FIG. 22. Isoscaling parameter as a function of symmetry energy with modified secondary de-excitation. SMM calculated isoscaling parameter α as a function of symmetry energy coefficient for various excitation energies. The open circles connected by dotted lines represent the primary fragments and the open stars connected by solid lines represent the secondary fragments. The right column shows the calculation for the ^{40}Ar+^{58}Fe/^{40}Ca+^{58}Ni system and the left column the ^{40}Ar+^{58}Ni/^{40}Ca+^{58}Ni system.

To better understand the difference in symmetry energy, figure 23 shows how the calculated isotopic yield distributions for carbon in the $^{40}Ar+^{58}Fe$ reaction at E^* = 6 MeV/nucleon compare. The left column in the figure corresponds to the SMM calculations where the fragment masses used are those of cold isolated nuclei, whereas, the right column corresponds to the SMM calculations where the masses evolve with their excitation energy during secondary de-excitation. The top panels and bottom panels are the primary and secondary yield distributions respectively. The dotted and solid curves shown in both top and bottom panels correspond to calculations that assume two different values of the symmetry energy, γ=15MeV (dotted curve) and γ=25MeV (solid curve) at an excitation energy of E^*=6MeV. Due to the difference of whether the mass (symmetry energy) evolves during the evaporation process or not, the bottom panels show the subtle difference in final (secondary) distributions at both values of γ. The SMM calculation with the standard de-excitation (i.e. the old de-excitation) leads to a narrow final distribution and the isotopes are concentrated close to the β-stability line. Overall, the difference in the final yield distributions for γ=15MeV and γ=25MeV is very small but much more prominent in the new de-excitation calculation. This can be seen in the secondary distribution by how the curves are considerably wider and shifted toward the neutron-rich side and therefore, it is shown that the SMM calculation that uses the modified secondary de-excitation with the evolving symmetry energy co-efficient produces a much larger yield distribution for neutron rich fragments. A similar observation was made by Buyukcizmeci *et al*. [62] in their calculation of the primary and secondary fragment isotopic distributions of ^{197}Au, ^{124}Sn and ^{124}La systems. By

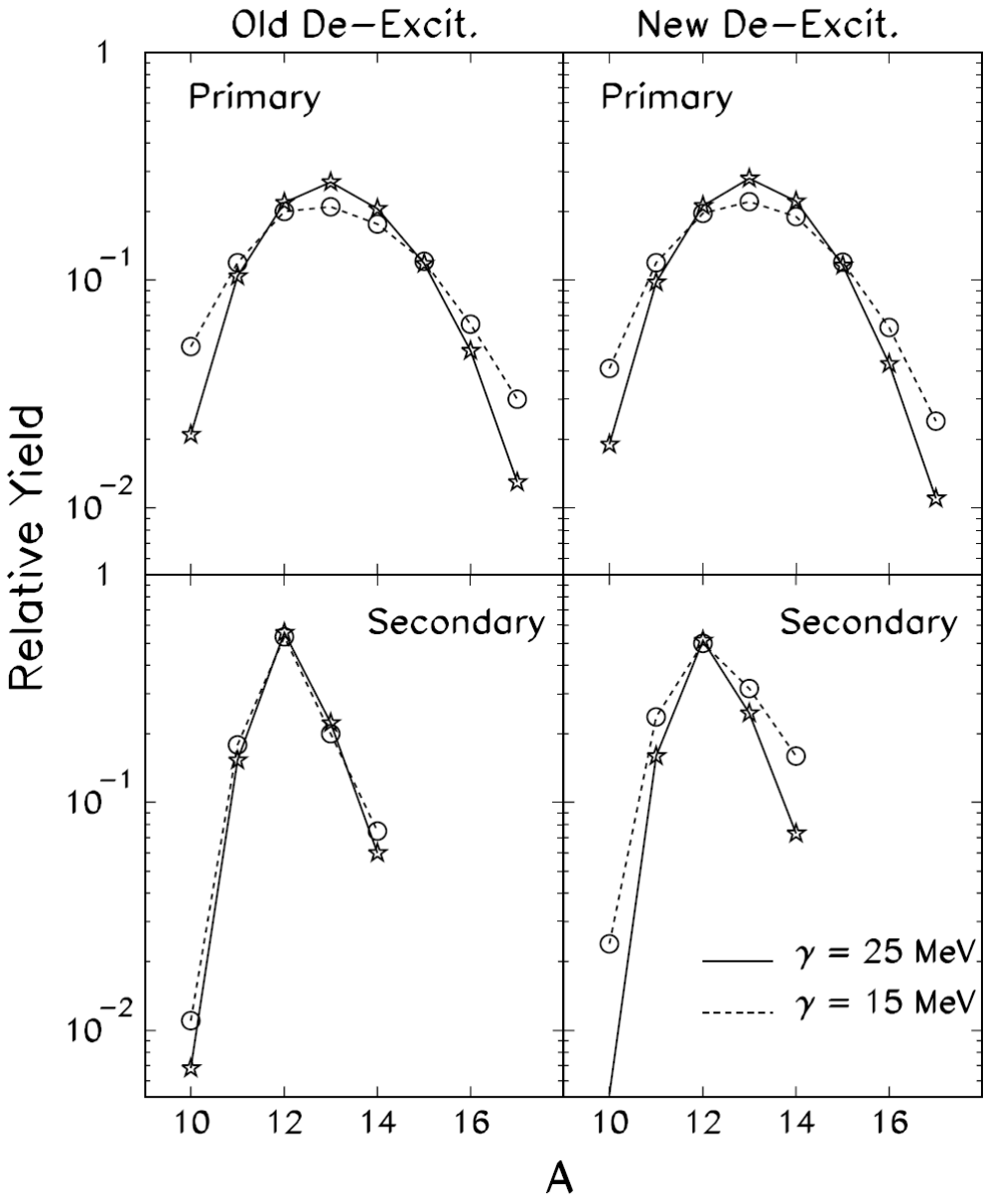

FIG. 23. Comparison between the two SMM calculations. The left panels represent the old SMM that uses the mass of the cold isotopes and the right panels represent the new SMM where the mass evolves with excitation energy during the secondary de-excitation. The top (primary) and bottom (secondary) panels show the isotopic yield distribution for the Carbon element in the ^{40}Ar+^{58}Fe reaction at E^*=6MeV/nucleon, while the solid and dashed curves correspond to the calculations using the two different values of the symmetry energy.

using the experimental masses during the evaporation process from the primary fragments, the emission of the charged particles is suppressed by the binding energy and the Coulomb barrier. In the case of small γ, the binding energy during the beginning of the evaporation process essentially favors the emission of charged particles to the point where the nucleus has cooled sufficiently. When it reaches this point normal symmetry energy has been reached and the remaining excitation energy is too low (E^*/A<1 MeV) for the nucleus to evaporate many neutrons resulting in more neutron rich fragmented particle yields.

The above comparison shows how both the experimentally observed data and the multifragmentation simulated data's final (secondary) fragment distribution depends very heavily on the available free energy and the strength of the symmetry energy, regardless of the secondary de-excitation. A significantly lower value of the symmetry energy than once assumed for cold isolated nuclei is required to explain the isotopic composition of the fragments produced in a multifragmentation reaction. The difference between the two kinds of evaporation calculations gives a measure of the uncertainty expected in the present analysis. The results above indicate that the properties of nuclei produced at high excitation energy, isospin and reduced density could be significantly different from those of the cold isolated nuclei. Such information can provide important inputs for the understanding of the nuclear composition of supernova mater where hot and neutron rich nuclei are routinely produced. [4,23]

SUMMARY AND CONCLUSIONS

In summary, the isotopic yield distributions of fragments produced in the multifragmentation reactions of ^{40}Ar, ^{40}Ca + ^{58}Fe, ^{58}Ni at 25-53 MeV/nucleon was measured. The symmetry energy and the isoscaling properties of the fragments produced were studied within the framework of the statistical multifragmentation model, and it is observed that the isoscaling parameter, α, for the hot primary fragments decreases as excitation energy increases and as symmetry energy decreases. The α values increase with increasing difference in the isospin of the fragmenting system. Similar behavior is also observed for the cold secondary fragments. The sequential decay of the primary fragments to the secondary fragments is observed to have very little influence on the isoscaling parameter as a function of excitation energy and isospin of fragmenting systems. The symmetry energy, however, strongly influences the isotopic comparison of the hot primary fragments. The experimentally determined scaling parameters could be explained by a symmetry energy that is as low as 13-15 MeV, which is significantly lower than that for the normal (cold) nuclei at saturation density. The present results indicate that the isospin properties of the fragments produced at high excitation energy and reduced density in multifragmentation reactions are sensitive to the symmetry energy.

Figure 24 compares the symmetry energy observed for the two reaction pairs, Ar+Ni / Ca+Ni and Ar+Fe / Ca+Ni (triangle symbols), with other recent data as a function of relative density and illustrates the agreement between the statistical and the

dynamical approach. With a lower value of symmetry energy and knowing that in a multifragmentation reaction the system expand to sub-nuclear density (about 1/3 the normal density as taken in the SMM calculation). It is observed that all these results are in agreement with a stiff form of the density dependence of the symmetry energy and can be written as Esym = $31.6(\rho/\rho_o)0.69$.

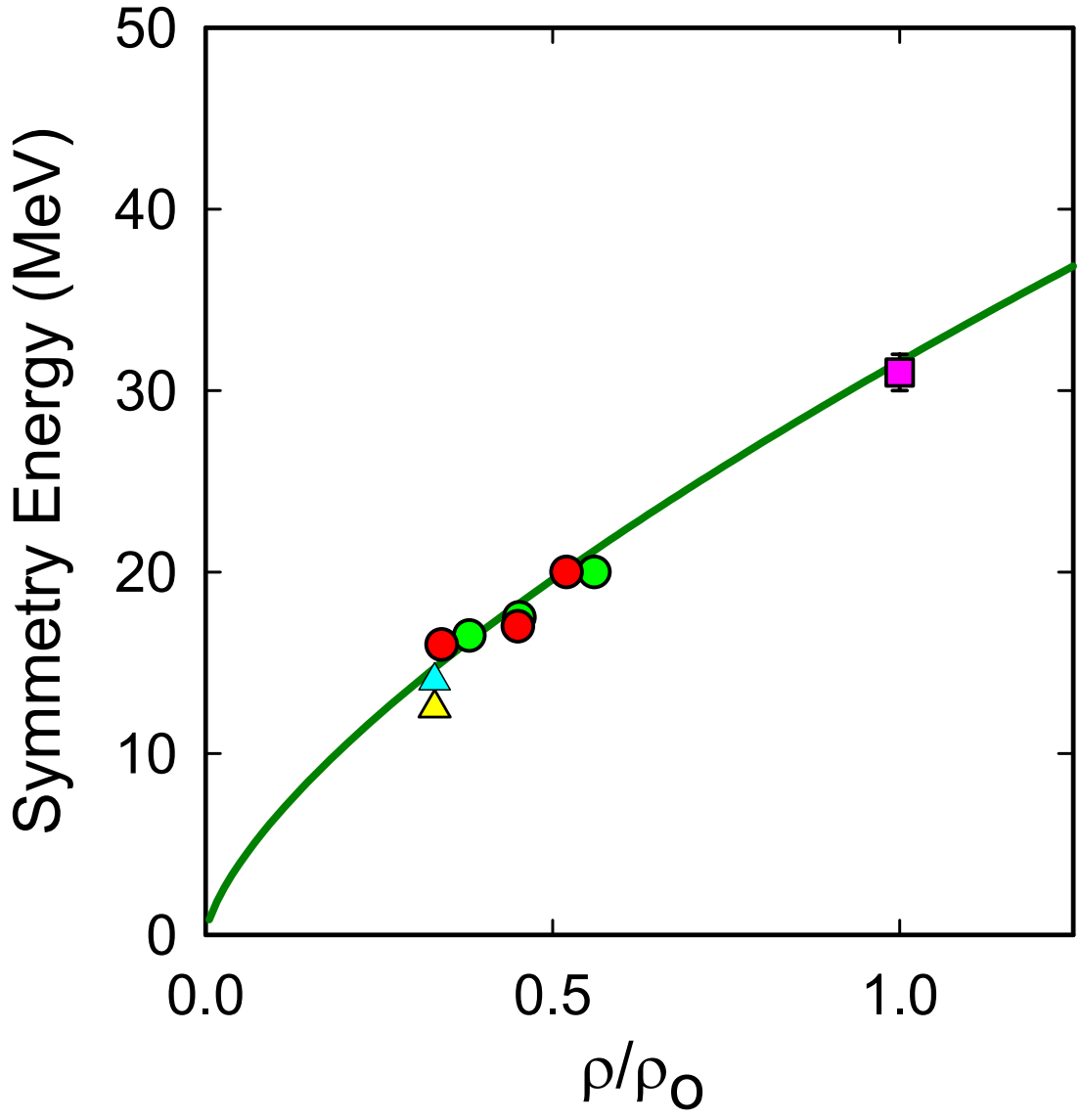

FIG. 24. At a reduced sub-nuclear density (about 1/3 the normal nuclear density), the symmetry energy as a function of the density of the present experimental data is represented by the two triangle symbols. The results from the present study correspond to a more stiff for form of symmetry energy and agree with data obtained by our group and others, shown by the circle and square symbols [63].

REFERENCES

[1] C. Fuchl, and H.H. Wolter. Eur Phys. J A **30**, 5 (2006).

[2] J. Stone, J.C. Miller, R. Koncewicz, P.D. Stevenson, and M.R. Strayer, Phys. Rev. C **68** 034324 (2003).

[3] J.P. Bondorf, R. Donangelo, I.N. Mishustin and H. Schultz, Nucl. Phys. A444, 460 (1985).

[4] D.V. Shetty, A.S. Botvina, S.J. Yennello, G.A. Souliotis, E. Bell, and A. Keksis, Phys. Rev. C **71**, 024602 (2005).

[5] A. LeFevre, G. Auger, M.L. Begemann-Blaich, N. Bellaize, R. Bittiger, *et al.*, Phys. Rev. Lett. **94**, 162701 (2005).

[6] D. Henzlova, A.S. Botvina, K.H. Schmidt, V. Henzl, P. Napolitani and M.V. Ricciardi, nucl-ex/0507003 (2005).

[7] A.S. Botvina and I.N. Mishustin, Phys. Lett. **B584**, 233 (2004).

[8] A.S. Botvina, O.V. Lozhkin, and W. Trautmann, Phys. Rev. C **65**, 044610 (2002).

[9] L.M. Lattimer, C.J. Pethick, M. Prakash, and P. Hansel, Phys. Rev. Lett. **66**, 2701 (1991).

[10] C. Lee, Phys. Rep. **275**, 255 (1996).

[11] C.J. Pethick and D.G. Ravenhall, Annu. Rev. Nucl. Part. Sci. **45**, 429 (1995).

[12] J.M. Lattimer and M. Prakash, Phys. Rep. **333**, 121 (2000).

[13] W.R. Hix, O.E.B. Messner, A. Mezzacappa, M. Liebendorfer, J. Sampaio, K. Langanke, D.J. Dean, and G. Martinez-Pinedo, Phys. Rev. Lett. **91**, 201102 (2003).

[14] J.M. Lattimer and M. Prakash, Astrophys. J. **550**, 426 (2001).

[15] A.S. Botvina, and I.N. Mishustin, Phys. Rev. C **72**, 048801 (2005).

[16] B.A. Brown, Phys. Rev. Lett. **85**, 5296 (2000).

[17] C.J. Horowitz and J. Piekarewicz, Phys. Rev. Lett. **86**, 5647 (2001).

[18] R.J. Furnstahl, Nucl. Phys. **A706**, 85 (2002).

[19] K. Oyamatsu, I. Tanihata, Y. Sugahara, K. Sumiyoshi, and H. Toki, Nucl. Phys. **A634**, 3 (1998).

[20] A. Ono, P. Danielewicz, W.A. Friedman, W.G. Lynch, and M.B. Tsang, Phys. Rev. C **68**, 051601 (2003).

[21] L.W. Chen, C.M. Ko, and B.A. Li, Phys. Rev. Lett. **94**, 032701 (2005).

[22] D.V. Shetty, S.J. Yennello, A.S. Botvina, G.A. Souliotis, M. Jandel *et al.*, Phys. Rev. C **70**, 011601(R) (2003).

[23] M.B. Tsang, T.X. Liu, L. Shi, P. Danielewicz, C.K. Gelbke *et al.*, Phys. Rev. Lett. **92**, 062701 (2004).

[24] B.A. Li, C.M. Ko, and W. Bauer, Int. J. Mod. Phys. E **7**, 147 (1998).

[25] V. Baran, M. Colonna, V. Greco, and M. DiToro, Phys. Rep. **410**, 335 (2005).

[26] V. Baran, M. Colonna, M. DiToro,V. Greco, M. Zielinska-Pfabe, and H.H. Wolter, Nucl. Phys, **A703**, 603 (2002).

[27] T.X. Liu, M.J. van Goethem, X.D. Liu, W.G. Lynch, R. Shomin *et al.*, Phys. Rev. C **69**, 014603 (2004).

[28] D. Lunney, J.M. Pearson, and C. Thibault, Rev. Mod. Phys. **75**, 1021 (2003).

[29] A.E.L. Dieperink, Y. Dewulf, D. Van Neck, M. Waroquier, and V. Rodin, Phys. Rev. C **68**, 064307 (2003).

[30] W. Zuo, I. Bombaci, and U. Lombardo, Phys. Rev, C **60**, 024605 (1999).

[31] M. Brack, C. Guet, and H.B. Hakansson, Phys. Rep. **123**, 276 (1985).

[32] J.M. Pearson and R.C. Nayak, Nucl. Phys. **A668**, 163 (2000).

[33] W.K. Myers and W.J. Swiatecki, Nucl. Phys. **81**, 1 (1966).

[34] K. Pomorski and J. Dudek, Phys. Rev. C **67**, 044316 (2003).

[35] H. Johnston, T. White, B.A. Li, E. Ramakrishnan, J. Winger *et al.*, Phys. Rev. C **56**, 1972 (1997).

[36] S.J. Yennello, B. Young, J. Yee, J.A Winger, J.S. Winfield *et al*., Phys. Lett. **B321**, 15 (1994).

[37] R.P. Schmitt, L. Cooke, G. Derrig, D. Fabris, B. Hurst, J.B. Natowitz, G. Nebbia, D. O'Kelly, B.K. Srivastava, W. Turmel, D. Utley, H. Utsunomiya, and R. Wada, Nucl. Instrum. Methods Phys. Res. A **354**, 487 (1995).

[38] C.A. Ogilvie, D.A. Cebra, J. Clayton, S. Howden, J. Karn, A. Vander Molen, G.D. Westfall, W.K. Wilson, and J.S. Winfield, Phys. Rev. C **40**, 654 (1989).

[39] S.J. Yennello, *Proceedings of the 10th Winter Workshop on Nuclear Dynamic, Snowbird, UT,* edited by W. Bauer (1994).

[40] M.B. Tsang , C.K. Gelbke, X..D. Lui, W.G. Lynch, W.P. Tan *et al.*, Phys. Rev. C **64**, 054615 (2001).

[41] M.B. Tsang, W.A. Friedman, C.K. Gelbke, W.G. Lynch, G. Verde, and H. Xu, Phys. Rev. Lett. **86**, 5023 (2001).

[42] A.R. Raduta, Eur. Phys. J. A **24**, 85 (2005).

[43] M.B. Tsang, W.A. Friedman, C.K. Gelbke, W.G. Lynch, G. Verde, and H. Xu, Phys. Rev. C **64**, 041603(R) (1985).

[44] S. Albergo *et al*., Nuovo Cimento A **89**, 1 (1985).

[45] J.P. Bondorf, A.S. Botvina, A.S. Iljinov, I.N. Mishustin and K. Sneppen, Phys. Rep. **257**, 133 (1995).

[46] J. Randrup and S. Koonin, Nucl. Phys. A **356**, 223 (1981).

[47] A.S. Botvina, A.S. Iljinov, I.N. Mishustin, J.P. Vondorf, R. Donangelo and K. Sneppen, Nucl. Phys. A **475**, 663 (1987).

[48] D.H.E. Gross, Rep. Progr. Phys. **53**, 605 (1990).

[49] D.H.E. Gross, L. Satpathy, Meng Ta-chung, and M. Satpathy, Z. Phys. A **309**, 41 (1982).

[50] X.Z. Zhang, D.H.E. Gross, S. Xu, and Y.M. Zheng, Nucl. Phys. A **461**, 641 (1987).

[51] M. D'Agostino, A.S. Botvina, P.M. Milazzo, M. Bruno, G.J. Kunde *et al.*, Phys. Lett. **B371**, 175 (1996).

[52] A.S. Botvina, I.N. Mishustin, M. Begemann-Blaich, J. Hubele, G. Imme *et al*., Nucl. Phys. A **584**, 737 (1995).

[53] R.P. Scharenberg, B.K. Srivastava, S. Albergo, F. Bieser, F.P. Brady *et al*., Phys. Rev. C **64**, 054602 (2001).

[54] N. Bellaize, O. Lopez, J.P. Wieleczko, K. Cussol, G. Auger *et al*., Nucl. Phys. A **709**, 367 (2002).

[55] S.P. Avdeyev, V.A. Karnaukhov, L.A. Petrov, V.K. Rodionov, P.A. Rukoyatkin *et al*., Nucl. Phys. A **709**, 392 (2002).

[56] J. Pochodzalla, T. Mohlenkamp, T. Rubehn, A. Schuttauf, A. Worner *et al*., Phys Rev. Lett. **75**, 1040 (1995).

[57] M. D'Agostino, A.S. Botvina, M. Bruno, A. Bonasera, J.P. Bondorf *et al*., Nucl. Phys. A **650**, 329 (1999).

[58] A.S. Botvina and I.N. Mishustin, Phys. Rev. C **63**, 061601 (2001).

[59] D. Cussol, G. Bizard, R. Brou, D. Durand, M. Louvel *et al*., Nucl. Phys. A **561**, 298 (1993).

[60] B.A. Li, C.M. Ko, and Z. Ren, Phys. Rev. Lett. **78**, 1644 (1997).

[61] V. Baran, M. Colonna, M. DiToro, V. Greco, M. Zielinska-Pfabe and H.H. Wolter, Nucl. Phys. **A703**, 603 (2002).

[62] N. Buyukcizmeci, R. Ogul, and A.S. Botvina, Eur. Phys. J. A **25**, 57 (2005).

[63] D.V. Shetty, S.J. Yennello, G.A. Souliotis, A.L. Keksis, S.N. Soisson, B.C. Stein, and S. Wuenschel, Phys. Rev. C (2007) (submitted).

VITA

Name: Jennifer Ann Iglio

Address: Attn: Sherry Yennello
Cyclotron Institute
Texas A&M University
MS 3366
College Station, Texas, 77843-3366

Education: Master of Science, Chemistry
Texas A&M University
College Station, Texas
May, 2007

Batchelor of Science, Chemical Engineering
Texas A&M University
College Station, Texas
May, 2003